Synthesis of ZnO Nanowires and Applications as Gas Sensors

A Thesis Submitted to the College of

Graduate Studies and Research

In partial Fulfillment of the Requirements

For the Degree of Master of Science

In the Department of Chemistry

University of Saskatchewan

Saskatoon

By

Mintang Liu

PERMISSION TO USE

In presenting this thesis in partial fulfillment of the requirements for a post-graduate degree from University of Saskatchewan, it is agreed that the Libraries of this University may make it freely available for inspection. Permission for copying of this thesis in any manner, in whole or in part, for scholarly purposes may be granted by the professors who supervised this thesis work or, in their absence, by the Head of the Department of Chemistry or the Dean of the College of Graduate Studies and Research at the University of Saskatchewan. Any copying, publication, or use of this thesis, or parts thereof, for financial gain without the written permission of the author is strictly prohibited. Proper recognition shall be given to the author and to the University of Saskatchewan in any scholarly use which may be made of any material in this thesis.

Request for permission to copy or to make any other use of material in this thesis in whole or part should be addressed to:

Head of the Department of Chemistry

University of Saskatchewan

110 Science Place, Saskatoon, S7N 5C9

Saskatchewan, Canada

ABSTRACT

Gas sensors are devices that can convert the concentration of an analyte gas into an electronic signal. Zinc oxide (ZnO) is an important n-type metal oxide semiconductor which has been utilized as sensor for several decades. In recent years, there have been extensive investigations of nanoscale semiconductor gas sensors. The size reduction of ZnO sensors to nanometer scale provides a good opportunity to dramatically increase their sensing properties in comparison with their macroscale counterparts.

In this work, two kinds of ZnO nanostructures (nanowires and nanorods) were studied. ZnO nanowires were synthesized by electrodeposition while porous anodic aluminum oxide served as a growth template. Three types of ZnO nanowires with different diameters were obtained. Meanwhile, ZnO nanorods were prepared by a hydrothermal route from ZnO nanoparticle seeds. However, the aspect ratio (length/width) of nanorods was significantly smaller than that of nanowires. Both nanowires and nanorods were characterized by optical microscopy, scanning electron microscopy, powder X-ray diffraction, energy dispersive X-ray spectroscopy and energy dispersive spectroscopy.

The sensing performance of the synthetic ZnO nanostructures were investigated by three gases: saturated water vapour in air, saturated ethanol vapour in air, and carbon monoxide in air. Both ZnO nanostructures showed good sensitivity and selectivity to ethanol vapour. At high temperature, the ZnO nanosensors were up to seven times more responsive to ethanol vapour than water vapour and over 200 times more responsive to ethanol vapour than CO. Due to the size dependence, ZnO nanowires with the smallest diameter is considered the best sensor candidate among ZnO nanowires.

On the basis of previous work, Au/ZnO/Au multimetallic nanobarcodes were also synthesized by electrodeposition, and their sensing characteristics are to be investigated in the future.

ACKNOWLEDGEMENT

It has been a wonderful experience to work under the supervision of Professor Robert W. J. Scott, Department of Chemistry, University of Saskatchewan (Saskatoon, SK). His enthusiasm and patience helped me get through the periods of frustration associated with ups and downs of this work. I would like to express my sincere thanks and gratitude to him for his active guidance, kind interest and for helping me in variety of ways throughout the course of this work.

My sincere thanks are to my committee member, Prof. Jens Mueller, for his valuable suggestions and advice. Furthermore, I would like to express my sincere thanks to Dr. Stephen G. Urquhart, Mr. Tom Bonli from Department of Geological Science and Ms. Lauren Drake from University of Regina for giving me the permission to use instrumental facilities for the sample characterization.

I would also like to thank the present and past members of my research group Priya, Zahid, Wenbo, Tesfa, Wendy, Nicole, Mita, Adam, Toby, and Gina for their cooperation. I am also thankful to Yin Lu, for her help and constant encourage.

I would like to thank NSERC and University of Saskatchewan for granting the research project (to Dr. Scott) and financial assistant without which the work would not have been possible to carry out.

I want to thank my parents for their love and support; they are always standing by me throughout my life.

TABLE OF CONTENTS

LIST OF TABLES

LIST OF FIGURES

LIST OF ABBREVIATION

APCVD	atmospheric pressure CVD
AAO	anodic aluminum oxide
CBE	chemical beam epitaxy
CNT	carbon nanotube
CVD	chemical vapour deposition
DC	direct current
EDS	electron diffusion spectroscopy
EDX	energy dispersive X-ray spectroscopy
HMTA	hexamethylenetetramine
IDA	interdigitated array
LPCVD	low-pressure chemical vapour deposition
MOCVD	metal-organic chemical vapour deposition
MOS	metal oxide semiconductor
PANI	polyaniline
PLD	pulsed laser deposition
PVD	physical vapour deposition
PVP	polyvinylpyrrolidone
rps	round per second
SEM	scanning electron microscopy
TMA	trimethylamine
UV	ultraviolet
UV-Vis	ultraviolet-visible
VPE	vapour phase epitaxy
VLS	vapour-liquid-solid
VSLE	vapour-liquid-solid epitaxial

XRD	X-ray diffraction

CHAPTER 1

INTRODUCTION

1.1 Introduction to Gas Sensors

Gas sensors are devices that can change the concentration of an analyte gas into an electronic signal,[1] and are an important component of devices commonly known as "electric noses".[2] Instead of analyzing all of the individual gas constituents by techniques such as gas chromatography, optical spectroscopy, or mass spectrometry, gas sensors look for specific patterns or fingerprints of the response of different materials to the gas mixture.

The history of gas sensors can be traced back to the last century. Miners are among the first groups that became aware of the importance of detecting hazardous gases in their working environment; In the early years, small animals, such as birds, were used as a poor substitute for a quantifiable method to measure this hazard.[3] Another spur to the development of modern atmospheric testing devices is the atmospheric hazards within enclosed spaces, like ships. In 1927, Oliver W. Johnson introduced a portable, explosive gas indicator, which is now considered the first commercial gas sensor.[4]

In the past eighty years, scientists have developed various gas sensors such as electrochemical sensors, catalytic combustion sensors, infrared sensors, and diffusion fuel cell sensors.[4] These sensors have a broad range of applications in chemical engineering, medical, agriculture, architecture and other fields. In the past century, for commercial applications, there are several major types of gas sensors that have been developed.[4] The first are electrolyte-based potentiometric sensors for automobile exhaust monitoring, based on materials such as ZrO_2-Y_2O_3 solid oxide. ZrO_2-Y_2O_3 solid electrolytes can also be used as current limiting sensors, and are designed for the incomplete burn conditions in automobiles. Another important type of commercial sensor is the metal oxide semiconductor gas sensor, e.g. SnO_2, which uses changes in resistance of the metal oxide to detect low concentrations of gases.

The basic principles behind the operation of all the gas sensors are the sensitivity, selectivity, and reversibility of their sensing response. These terms can be defined in accordance with measurable parameters. The *sensitivity* of a sensor is a measure of the lowest concentration of an analyte gas that can be detected. The sensitivity can be calculated with respect to the mean

baseline response of the sensor, which is exposure to room air, relative to its response to a particular analyte gas concentration. Eq 1.1 shows the normalized sensitivity of the sensor operating under a fixed set of physical operating conditions,

$$\text{Sensitvitity}_{X(P)} = \left|\frac{X_{baseline} - X_{gas}}{X_{baseline}}\right| \quad (1.1),$$

where X is the mean value of a particular measured parameter while p for a specific set of data.

Selectivity is a measure of the sensors' ability to recognize one gas amongst others. The selectivity of the sensor can be determined by comparing the measurable parameters for each analyte gas. Eq 1.2 describes the selectivity of the sensor for an analyte gas (a) relative to another analyte gas and (b) with the same concentration,

$$\text{Selectivity}_{X(P)} = \left|\frac{X_{gas(a)} - X_{gas(b)}}{X_{gas(a)}}\right| \quad (1.2)$$

The *reversibility* parameter describes the sensors' ability to return to its initial state after it has been exposed to a particular analyte gas. The reversibility performance of the sensor is quantified with respect to time.[5]

1.2 Metal Oxide Semiconductor Gas Sensors

Metal oxide semiconductor (MOS) is one of the most important materials that could be applied for gas sensing measurements. It was first discovered decades ago that molecules interacting with semiconductor surfaces can influence the surface properties of semiconductors, such as conductivity and surface potential. The first chemoresistive semiconductor gas sensors were produced by Seiyama in 1962.[6] Since then, metal oxide semiconductors have been widely studied as gas sensors because of their low cost and relative simplicity. Metal oxides possess a broad range of electronic, chemical and physical properties that are often highly sensitive to the changes in their chemical environment. Due to these properties, metal oxides have become one the most popular commercial sensors. Numerous materials have been reported to be usable as metal oxide sensors including both single-component metal oxides such as ZnO, SnO_2, WO_3, TiO_2 and Fe_2O_3; and multi-component oxides, such as $BiFeO_2$, $MgAl_2O_4$, and $SrTiO_3$.[7]

1.2.1 Sensitivity and selectivity of semiconductor gas sensor

The key characteristics of semiconductor gas sensor performance are sensitivity, selectivity, response time and recovery time. For metal oxide semiconductors, the measurable parameter is the resistance of the metal oxide, thus the sensitivity of the semiconductor is defined as follows,[8]

$$\text{Sensitvitity } (S_g) = \frac{R_{gas}}{R_{air}} \quad (1.3),$$

where R_{air} the resistance of the sensor in air; and R_{gas} is the resistance of the sensor after exposure to the analyte gas. Using this definition of sensitivity, the sensitivity is easily calculated from the measured resistance values. Thus, it is very convenient to compare the sensitivities in different substrate gas environments.

The sensitivity of semiconductor gas sensors can also be empirically represented as,[9]

$$S_g = A \times P_g^{\beta} \quad (1.4),$$

where P_g is partial pressure, which is directly proportional to its concentration of the target gas. The sensitivity is characterized by the pre-exponential factor A and the exponent β. β may have some rational fraction value (usually 1 or 1/2), depending on the charge of the surface species and the stoichiometry of the elementary reactions on the surface.

The selectivity of metal oxide semiconductors is defined as the ratio of the sensitivity of one analyte gas relative to another analyte gas under same conditions.[10] Semiconductor gas sensors often exhibit poor selectivity since their operation depends, in most cases, on the reaction of reducing gases with adsorbed oxygen (see next section for mechanistic discussion).

$$\text{Selectivity}_{S_{(P)}} = \left|\frac{S_{gas(a)} - S_{gas(b)}}{S_{gas(a)}}\right| \quad (1.5)$$

The response time and recovery time are usually defined as the time taken to achieve 90% of the final change in resistance following the change of gas concentration (τ_{90}). However, as the gas sensor response is often very fast initially, followed by a long drawn out tail before reaching a steady value, response times are alternatively often expressed as 50% or 70% of the final time.[11] The response time is an important parameter since it can determine the commercial applicability of the sensor; unfortunately, it is probably the most difficult parameter to measure

in a reproducible manner. It requires special gas flow systems which are designed to ensure that step changes in gas concentration are faster than the response time of the sensor, especially when dealing with highly adsorptive and reactive gases. The commercial usage of a gas sensor is highly dependent on its recovery time; a gas sensor that has a short recovery time will have greater applications in the commercial market than one with a long recovery time.

1.2.2 Applications of semiconductor gas sensors

Numerous kinds of gases are emitted from various sources into our living space, working space, and outdoors. Many of them are hazardous to human beings and the environment. Most of the gases are present at very low concentrations so that extremely sensitive sensors are required for their monitoring. Metal oxide semiconductors are considered as one of the most promising gas sensor candidates. Since the first semiconductor gas sensor was created in 1960's,[6] much technological effort has been made to improve semiconductor gas sensors, in particular aiming at improve their sensitivity, selectivity, stability, and convenience for practical use. Nowadays, semiconductor gas sensors are widely used for domestic and industrial gas detectors, gas-leak alarms, process control and pollution control. In addition, semiconductor gas sensors have been successfully employed as sensors for the detection of different gases, such as CO, CO_2, H_2, alcohol, H_2O, NH_3, O_2, NO_x, and liquid petroleum gas (LPG). [12]

1.2.3 Response mechanism

The sensing mechanism of a sensor is that their properties vary with the environment changes, and it is easier to us to monitor the property varies than the concentration of the gases. To the semiconductor, the electronic property changes in the oxidation and reduction gases. The process of gas sensing with a metal oxide semiconductor involves two key functions: one is the recognition of a target gas through a gas-solid interaction, which induces an electronic change of the oxide surface, commonly referred to as a receptor function; the other is transduction of the surface phenomenon into an electrical resistance change of the sensor, which is referred to as a transducer function. Although the following discussion focuses on the sensing mechanism of nanocrystalline zinc oxide, the actual mechanism can also be applied to a large number of metal

oxides.[13] The receptor function of a gas sensor is provided by the surface chemical properties of the metal oxide semiconductor to adsorb or react with the analyte gas.

One of the typical metal oxide semiconductor is ZnO, we utilize ZnO as an example to discuses the sensing mechanism. Let us first consider a ZnO surface exposed to normal air conditions. Oxygen is one the most active components in air and the amount of oxygen in air is approximately 20.9% by volume. Oxygen vacancies on metal-oxide surfaces are electrically and chemically active. Metal oxides are often naturally self-passivated against oxygen as there is always oxygen adsorbed to the metal oxide gas surface when the surface is exposed to air. The oxygen molecule can bind to vacancy sites on the metal oxide surface, and trap electrons from the surface of the metal oxide, as shown in Figure 1.2. It then remains tightly bound as a charged oxygen anion. The trapped electron is no longer available for conductivity in the solid, thus increasing the resistance of the oxide surface. These processes can be represented by the following reactions,[14,15]

$$O_{2(gas)} \rightarrow O_{2(ads)} \tag{1.6}$$

$$O_{2(ads)} + e^- \rightarrow O^-_{2(ads)} \tag{1.7}$$

$$O^-_{2(ads)} + e^- \rightarrow 2\,O^-_{(ads)} \tag{1.8}$$

$$2\,O^-_{(ads)} + e^- \rightarrow O^{2-}_{(ads)} \tag{1.9}$$

In these surface reactions, (gas) and (ads) stands for free gas and species adsorbed on the surface respectively, e^- stands for electrons contributed by ZnO. $O_2^-{}_{(ads)}$, $O^-_{(ads)}$ and $O^{2-}_{(ads)}$ stand for the different physisorbed and chemisorbed surface oxygen species. Reactions (1.7) - (1.9) are known to be triggered in turn at increasing temperatures: the $O_2^-{}_{(ads)}$ is the major oxygen species below 150 ℃ and $O^{2-}_{(ads)}$ becomes dominant when the temperature is above 450 ℃; while when the temperature is in the range of 150 ℃ to 450 ℃, $O^-_{(ads)}$ plays the major role.[14,16] Metal oxide gas sensors are commonly operated at elevated temperatures (250 – 500 ℃) in order to achieve enhanced chemical reactivity between the sensor materials and the analyte gases, primarily due to the formation of oxygen anions at these temperatures as discussed above.

When the solid state gas sensor is exposed to air at elevated temperatures, the surface is covered by oxygen anions and a space-charge layer is formed on the surface of the metal oxide, as shown in Figure 1.1. The space-charge layer is a region that has deficient carriers due to electron trapping by the chemisorbed oxygen. A typical value of the space-charge thickness (Debye thickness, or Debye length) is 30 nm for undoped ZnO.[17] When n-type semiconductor gas sensors are exposed to air, the resistance of the sensors increases with respect to the vacuum reference value, as the high resistance at grain boundaries leads to a lower conductivity through the whole oxide, as shown in Figure 1.2.

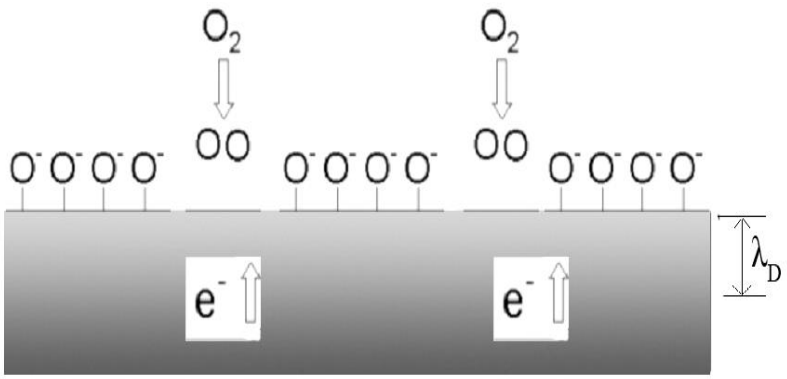

Figure 1.1 Schematic description of the chemisorption of O_2 on the surface of a metal oxide gas sensor.[16]

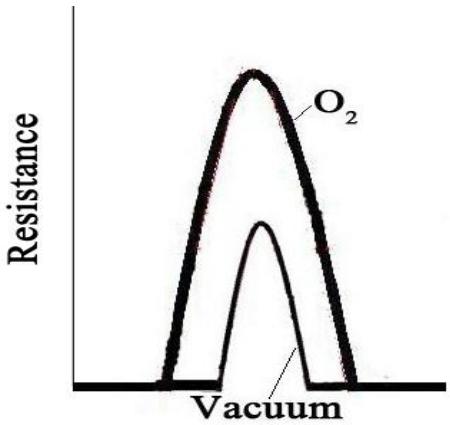

Figure 1.2 Schematic description of resistance change when O_2 adsorbs to a metal oxide surface.

Other gases in the atmosphere can also lead to changes in the resistance of the metal oxide materials – below is a discussion of the behaviour of metal oxide surfaces to water vapour, CO, and alcohol vapour.

1.2.3.1 Water vapour

The water content in surrounding air, in terms of humidity and moisture, is an important factor for the well-being of humans and animals. It is also a significant factor for operating certain equipment such as electrostatic-sensitive components. Thus, humidity sensors have important applications in industrial processing and environmental controls.[18]

H_2O vapour can be adsorbed on metal oxide surfaces in both molecular and hydroxyl forms, and thus competes with O_2 for oxygen vacancy sites on the oxide surface, as shown in Figure 1.3. This competition for oxygen vacancy sites will also lead to changes the conductivity of the metal oxide sensor.[18] When ZnO sensors are operating in humid conditions, the H_2O molecules occupy some of the O vacancies, leading to a lower chemisorption of O_2 on the oxide surface; thus, fewer electrons are trapped by oxygen anions. This leads to an increase in the conductivity of ZnO sensors resulting from a decrease in the energy barriers between metal oxide grains.[19]

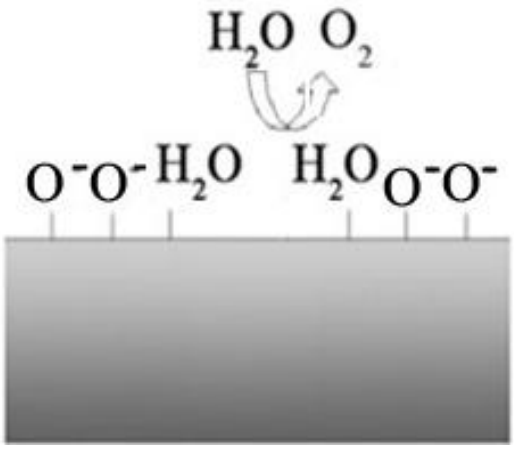

Figure 1.3 Schematic description of the sensing mechanism of water vapour on the surface of a metal oxide gas sensor.

1.2.3.2 Carbon monoxide

Carbon monoxide (CO) is one of the most dangerous and fatal gases in air pollution.[8] CO is mainly produced by incomplete combustion of fuels and commonly found in the emission of automobile exhausts and the burning of domestic fuels. It is highly toxic and extremely dangerous because it is colourless and odourless. CO sensors are, therefore, required by law in many locations, particularly for the detection of smouldering fires.

The sensitivity of ZnO semiconductor gas sensors to reducing gases such as CO is attributed to the chemisorption of oxygen on the sensor surface and the subsequent reaction between adsorbed oxygen anion species and the analyte gas. Thus when a ZnO sensor is placed in a carbon monoxide gas atmosphere, CO molecules react with the pre-adsorbed oxygen species. The reaction is as follows[8]:

$$CO_{(gas)} + O^-_{(ads)} = CO_{2(gas)} + e^- \quad (1.10)$$

As a result, the surface oxygen concentration is reduced, and electrons that were initially trapped by oxygen anions are released back into the ZnO solid, leading to an increase in the conductivity of the sensor, as shown in Figure 1.4.

The mechanism of metal oxide sensor response to carbon monoxide is also applicable for other reducing gas such as hydrogen. Meanwhile, ZnO sensors can also be utilized to detect oxidizing gases, such as ozone, which trap electrons on the surface to produce oxygen anions, leading to a decrease in conductivity of the material. However, in general, it is easier to accurately measure the conductivity changes than to detect the decrease of concentration of the gases.

Harrison and Willett[20] applied transmission infrared spectroscopy to monitor the sensing reaction. They assumed that the reaction included the CO adsorption and desorption of CO_2. Their work illuminated that the adsorption sites for CO involve surface oxygen anions. Figure 1.5 shows the structure of the surface species formed. The reaction of CO with adjacent pairs of oxygen anions produced surface bidentate carbonate species as seen in Figure 1.5 (a). The bidentate carbonate species subsequently transforms into surface unidentate carbonate, 1.5 (b). The adsorption of CO at a single oxygen anion site then yields surface carboxylate groups.

During the formation of all these surface species, there is no electron transfer to the bulk metal oxide sensor, thus no conductance change. However desorption of CO_2 provides opportunities for the electrons to return to the sensor solid. CO_2 desorption is favoured at higher temperatures, but not favoured at low temperatures.[20]

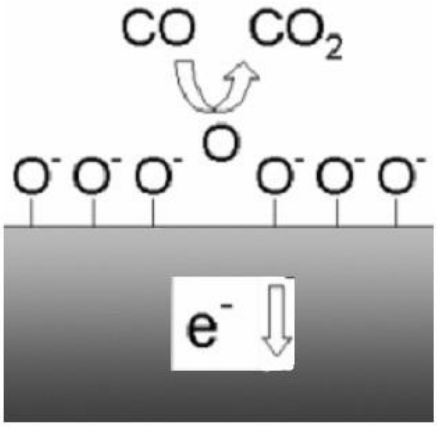

Figure 1.4 Schematic description of the sensing mechanism of carbon monoxide over the surface of metal oxide gas sensor.[14]

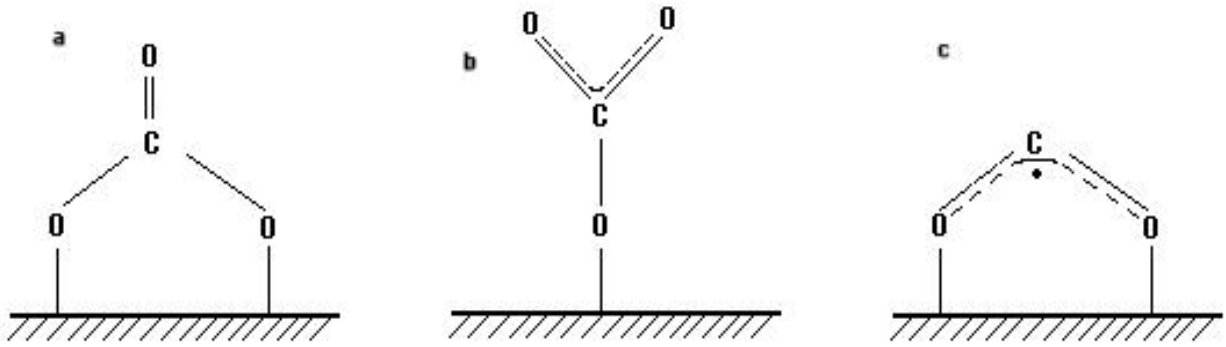

Figure 1.5 Structure of the surface species formed on metal oxide surfaces from a CO/air mixture. (a) bidentate carbonate; (b) unidentate carbonate; and (c) carboxylate.[20] (Adapted with permission from reference 20. Copyright 1998 Nature.)

1.2.3.3 Alcohol vapour

Accurate detection of alcohol vapour is another area of commercial importance. The most common application of alcohol sensors is to detect of ethanol vapour level in human breath (breathalyzer), which is correlated to the alcohol concentration in the blood. Gas sensors based on the metal oxide semiconductor have been found to be very useful for detecting ethanol vapour.[21]

The mechanism of ethanol detection by zinc oxide gas sensors can be explained by two-different oxidation pathways; the first pathway involves the oxidation of ethanol by dehydrogenation to form a CH_3CHO intermediate, and the second pathway involves the dehydration of ethanol to C_2H_4. The selectivity for these two reactions is determined by the acid-base properties of the metal oxide surface. The dehydrogenation process is more probable on basic oxide surfaces, while dehydration is favoured over acidic surfaces. In addition, dehydrogenation processes usually take place at higher temperatures than dehydration processes. The relevant reactions are as follows:[22,23]

$$CH_3\,CH_2\,OH_{\,(gas)} + [O]_{(ads)} \rightarrow CH_3\,CHO_{(ads)} + H_2O \qquad (1.11)$$

$$CH_3\,CH_2\,OH_{\,(gas)} + [O]_{(ads)} \rightarrow C_2H_4 + H_2O \qquad (1.12),$$

in which $O_{(ads)}$ represents the surface oxygen species.

Dr. Rao and co-workers have studied the mechanism of ethanol oxidation over ZnO surfaces.[22] At around 300 ℃, ethanol dehydrogenates to form the acetaldehyde (CH_3CHO) intermediate and produces an adsorbed hydrogen atom. The adsorbed hydrogen atoms then are oxidized over the ZnO surface. The generated protons associate with the surface-adsorbed oxygen ions forming $OH_{(ads)}$. Two adsorbed OH groups condense and eliminate one H_2O molecule, leaving an adsorbed oxygen anion. During the above dehydrogenation process, one net electron is released into the conduction band of ZnO, thus reducing its resistance (see eq 1.19). The overall dehydrogenation process is summarized as follows,[22]

$$CH_3\,CH_2\,OH_{\,(gas)} \rightarrow CH_3CH_2O_{(ads)} + H_{(ads)} \qquad (1.13)$$

$$CH_3\,CH_2\,O_{(gas)} \rightarrow CH_3CHO_{(ads)} + H_{(ads)} \quad (1.14)$$

$$H_{(ads)} + H_{(ads)} \rightarrow 2\,H^+_{(ads)} + 2\,e^- \quad (1.15)$$

$$2\,H^+_{(ads)} + 2\,O^-_{(ads)} \rightarrow 2\,OH_{(ads)} \quad (1.16)$$

$$2\,OH_{(ads)} \rightarrow H_2O_{(ads)} + O_{(ads)} \quad (1.17)$$

$$O_{(ads)} + e^- \rightarrow O^-_{(ads)} \quad (1.18)$$

The net reaction is:

$$CH_3\,CH_2\,O_{(gas)} + O^-_{(s)} \rightarrow CH_3CHO_{(ads)} + H_2O + e^- \quad (1.19)$$

The adsorbed acetaldehyde (CH_3CHO) intermediate can also undergo further oxidation to form acetate intermediates. This reaction is shown below (eq 1.20)[22]. The acetate intermediate $CH_3CO_{2(ads)}$ can then decompose into CO_2 and water vapour, however, details of the mechanism at this stage are still an active area of research. However, as oxygen anions on the surface are involved in the initial reaction, the trapped electrons are released, followed by a decrease in the resistance of the sensor. Figure 1.6 shows an overview of the sensor response of ZnO to ethanol vapour.

$$CH_3\,CHO_{(ads)} + O^-_{(s)} \rightarrow CH_3CO_{2(ads)} + e^- \quad (1.20)$$

In the past several years, although many studies have been carried out the sensing of hazardous gases like CO, there is a common problem in the area, which is the poor selectivity to specific gas. Common metal oxide sensors show responses for all three gases discussed above (water, CO, ethanol). This would be problematic, e.g. because CO detectors may show false signals due to high humidity and/or ethanol vapour. Thus sensors that have strong specific responses to one gas are highly desirable.

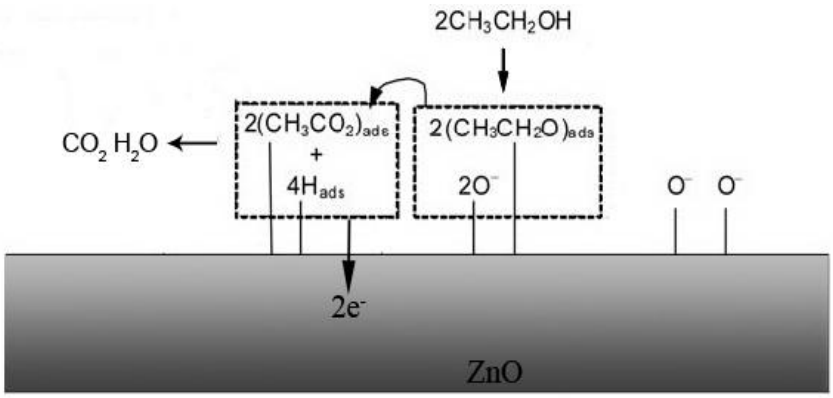

Figure 1.6 Schematic description of sensing mechanism of ethanol over the surface of a metal oxide gas sensor.

1.2.4 Zinc oxide semiconductor

Zinc oxide is an important semiconductor which has been studied for many decades. It has a wide band-gap of 3.37 eV and a large exciton binding energy of 60 meV at room temperature.[24] Polycrystalline ZnO has attracted intensive research effort for its unique properties and versatile applications in ultraviolet (UV) light emitters, short-wavelength nano-lasers, piezoelectric devices, ultrasensitive, spin electronics, field-effect transistors, and field emitters.[25] ZnO, like ZnS, has the wurtzite structure type, which is the thermodynamically stable phase under ambient conditions. The ZnO wurtzite structure has a hexagonal closed-packed unit cell, with dimensions a = 3.25 Å and c = 5.12 Å. The structure can be visualized as Zn^{2+} ions in half of the tetrahedral holes of a hexagonal close-packed oxide lattice; the structure with the longitudinal axis (c-axis) is shown in Figure 1.1. In this crystal structure, both zinc and oxygen ions are coordinated with four ions of the opposite charge with strong ionic binding. Due to the size differential of the ions, the ions fill about 44% of the total volume in a ZnO crystal, and leaving a relatively large free volume.[26-30] Some typical properties of ZnO are listed below in Table 1.1.

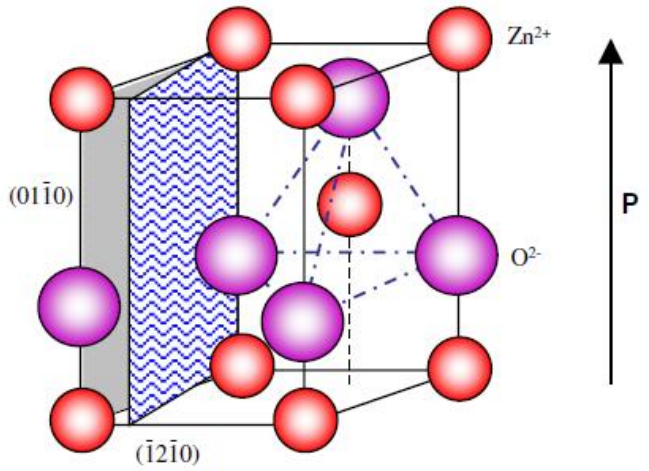

Figure 1.7 ZnO crystal: wurtzite structure, hexagonal close-packed arrangement of O atoms with Zn^{2+} in tetrahedral holes.[27] (Adapted with permission from reference 27. Copyright 2004 IOP Publishing Ltd.)

Crystal structure	Hexagonal, wurtzite
Molecular weight	81.38 g/mol
Lattice constant	a = 3.246 Å, c = 5.207 Å
Density	5.67 g/cm^3 or 4.21 x 10^{19} ZnO molecules/mm^3
Cohesive energy	E_{coh} = 1.89 eV
Melting point	Tm = 2250 ℃ under pressure
Heat of fusion	4, 470 cal/mole
Band gap at RT	3.37 eV
Exciton binding energy	E_b = 60 meV

Table 1.1 Selected properties of zinc oxide.[31]

Perfect ZnO single crystals can only be synthesized under high oxygen pressures and at relatively high temperatures. In ambient conditions, oxygen vacancies are a major defect in ZnO crystals. Due to the formation of oxygen vacancies in the structure upon heating, ZnO_{1-x} is a non-stoichiometric compound. Thus ZnO is a typical n-type semiconductor, in which the density of holes in the valence band is exceeded by the density of electrons in the conduction band; the major charge carrier in ZnO semiconductors is electrons in the conduction band.[31] The formation of oxygen vacancies leads to a higher electron density; donor bands from vacancies in the band gap lead to a substantial increase in the conductivity of the oxide.

The utilization of ZnO as a gas sensor has a long history because of its' chemical sensitivity to different adsorbed gases, high chemical stability, amenability to doping, non-toxicity, and low cost. Systems mainly composed of ZnO were studied as chemoresistive materials to detect gases like H_2, NH_3, CH_4, O_2, trimethylamine (common in seafood odours), ethanol and CO.[22,32-43] One of the attractive features of the n-type semiconductor is that the conductivity increases upon exposure to oxidizing gases, which make it easy to measure a conductivity change.

1.3 Nanoscale Gas Sensors

In order to improve commercial gas sensors, many approaches have attempted to modify the sensing properties of metal oxide semiconductor gas sensors in order to achieve higher sensitivity and selectivity. Enhancements of the sensing properties of MOS sensor materials can be achieved by the development of sensors with nanoscale sizes and structures, such as nanoparticles, nanowires, nanorods etc..[17] Quasi-one-dimensional MOS nanostructures, such as nanowires and nanorods, are expected to show higher sensitivity than bulk gas sensor for the following reasons: first, quasi-one-dimension nanostructures have a large surface-to-volume ratio, which means a significant fraction of the atoms in such systems are surface atoms that can participate in surface reactions, thus resulted into extremely sensitive to species adsorbed on their surfaces. Second, the radius of MOS nanowires is comparable to the Debye length λ_D through a wide temperature range, which causes their electronic properties to be strongly influenced by processes at their surfaces. Finally, semiconducting oxide nanowires are often stoichiometrically well defined and have a greater level of crystallinity than multi-granular oxides.[17] As the dimension of the semiconductor material shrinks down to the nanometer scale, some of their

physical properties undergo changes known as quantum size effects. For example, quantum confinement increases the band gap energy of quasi one-dimensional ZnO structures. Understanding the fundamental physical properties is crucial to the rational design of functional devices. Investigation of the properties of individual MOS nanostructures is essential for developing their potential as the building blocks for future nanoscale gas sensors.

When the size of zinc oxide structures is much larger than the Debye length λ_D (~ 30 nm for ZnO), only the atoms in the space-charge region can participate in surface reactions. Thus atoms in the core of ZnO crystals are not involved in the sensing response. Decreasing the size of a ZnO nanowire should thus result in a much larger portion of the ZnO wire which interacts with an analyte gas, which should increase the sensitivity of the sensor. When the size of ZnO nanowires is similar or smaller than the Debye length of ZnO, the sensitivity of the ZnO should increase dramatically. Figure 1.8 shows the relationship of Debye length and diameters of the sensors. With reducing diameter, the surface/volume ratio increases; and when the size of the wires is close to or even smaller than the Debye length, the whole wire can be treated as a surface. For the sensors based on the In_2O_3 nanowires, sensitivities up to 10^5-fold greater than those of comparable solid film devices have already been reported.[44] The signal-to-noise ratio obtained indicated that ~10^3 molecules can be reliably detected on a 3 μm-long device. By shortening the conductive channel length to ~ 30 nm, the adsorption of as few as 10 molecules could, in principle, be detected. [17,45]

Figure 1.8 Schematic description of size effect on the sensitivity of ZnO sensors.

1.3.1 Metal oxide semiconductor nanowires

1.3.1.1 Introduction of metal oxide semiconductor nanowires

The properties of nanostructured metal oxide semiconductors have been extensively studied in recent years. Several assortments of ZnO nanostructures, such as nanowires, nanorods, have been successfully grown via a variety of methods. [46] Our greatest interest has been focused on the cylinder-shaped nanowires. Nanowires are considered as ideal building blocks for constructing nanosized devices due to their high surface-to-volume ratios and physical and chemical properties resulting from their reduced size. Many semiconductor nanowires have been successfully applied as nanodevices, including nanolasers, nanogenerators, and various chemical and biological nanosensors.[45]

For most sensors, due to the limitation of surface area, an elevated temperature is needed to achieve high sensitivity and reversibility. Thus, sensors which have high sensor response at room temperature are desired by the commercial market. Xia and coworkers documented the synthesis of SnO_2 nanowires with a mean diameter of 50 nm and lengths up to 30 μm and showed that they exhibited both high sensitivity towards ethanol vapour and reversibility under ambient room temperature conditions.[47] The SnO_2 nanowires were synthesized by solution phase, as the precursor $SnC_2O_4 \cdot H_2O$ was dissolved in ethylene glycol mixed with poly(vinylpyrrolidone), then refluxed at an elevated temperature. The sensing study was carried out at room temperature; the resistance change of these SnO_2 nanowires was nearly 8,000 times upon exposure to 6% ethanol vapour in air; while for low concentration CO (20 ppm) and H_2 (500 ppm), the magnitude of the resistance change was about 3 for H_2 and ~ 4 for CO.[47]

In addition, Yang's group synthesized SnO_2 nanoribbons typically 80 ± 120 nm wide and 10 ± 30 nm thick, and showed adsorption-desorption behaviour of NO_2 at room temperature; commonly these reactions happen at high temperatures of 300 ℃ ~ 500 ℃ on bulk SnO_2 sensors. The SnO_2 nanoribbons were synthesized using thermal deposition process, in which commercial tin oxide powers were placed in an alumina crucible located in an alumina tube, and the source was evaporated and resulted into SnO_2 nanoribbons on alumina strip plates which were placed in the alumina tube. When illuminating the devices with ultraviolet (UV) light of energy near the SnO_2 band gap, the SnO_2 nanoribbons could detect ppm-level NO_2 at room temperature.[48]

Nanosized metal oxide semiconductors working as gas sensors have attracted a great deal of interests; Table 1.2 lists some of the papers focusing on the sensing properties of nanowires gas sensors based on metal oxide semiconductor (MOS) materials. From the table, it is apparent that MOS and metal-doped semiconductors can be used as sensors to detect a wide range of gases. For example, Rao and co-workers synthesized ZnO nanostructures with different route and studied the sensing property to detect H_2.[11] ZnO nanorods with 30 - 40 nm diameters and 600 - 800 nm lengths were synthesized by a hydrothermal route, and ZnO nanowires which had a diameter of 20 - 30 nm and length of 1 - 2 μm were prepared by an electrodeposition method. They also synthesized Pt-doped ZnO nanorods and nanowires. In the case of 1000 ppm H_2 at 150 ℃, they found that the pure ZnO nanorods showed a sensitivity towards H_2 of 32, while the Pt-doped nanorods had an enhanced sensitivity of 56. Meanwhile ZnO nanowires showed a sensitivity around 40 towards H_2, while Pt-doped ZnO nanowires showed nearly a 20 time increase in sensitivity. The sensing behaviour of both, the nanorods and nanowires, was also studied for 1000 ppm ethanol gas at 150 ℃; the ZnO nanorods showed a sensitivity towards ethanol of about 200, while Pt-doped ZnO nanorods had a response over 10 times higher, with a sensitivity of 2250. ZnO nanowires had a sensitivity towards ethanol of 300, compared to 480 for the Pt-doped nanowires.

Material	Structure	Size (nm)	Synthesis method	Gas	Temp. (℃)	S (Ra/Rg)	Ref.
ZnO	Nanorod	95	Hydrothermal	Ethanol benzene	450 150	100 10	[49]
ZnO	Nanorod	500	Hydrothermal	H_2 CO NH_3	250	8.5 2 5	[32]
ZnO	Nanorod	40-80	Hydrothermal (autoclave)	Ethanol	332	50	[50]
ZnO	NPs	10-20	Hydrothermal (autoclave)	Ethanol	350	20	[51]
ZnO	Thin film	50-500	Dip-casting	H_2 CH_4 H_2S	150	500 18 2	[52]
ZnO	Nanorod	37.5	Hydrothermal (autoclave)	NO_2 CO	350	1.8 1	[33]
ZnO	Thin Film	10	Sol-gel	Ethanol	RM	2.1	[53]
ZnO	Nanorod	100-800	CVD	Ethanol H_2S	100	6 2.3	[54]
ZnO	Nanowire	25	PECVD	Ethanol	300	47	[9]
ZnO Pt-ZnO	Nanorod Nanowire Nanorod Nanowire	30-40 20-30	Hydrothermal electrodeposition	H_2 Ethanol	150	36 200-300 2200	[11]
Cu-ZnO	Thin film	260	Deposition (PVD)	CO	350	5.5	[8]
ZnO Pd-ZnO	Thin film	500		H_2 LPG	300	1.67 500 4	[34]

Material	Structure	Size (nm)	Synthesis method	Gas	Temp. (℃)	S (Ra/Rg)	Ref.
ZnO Al-ZnO	Thin film	5000	Electrodeposition	H_2	150	150 120	[43]
Pd-ZnO+La_2O_3	Powder	2000-5000	Hydrolysis	Ethanol CO H_2	200	2 1.2 1.2	[22]
Sn_2O_3	Nanowire	30-300	Electrodeposition	CO H_2 NH_3	300	30%	[17]
SnO_2	Nanowire	60	Electrodeposition	CO	250	3	[14]
In_2O_3	Nanowire	10	Laser Ablation	NO_2	RM	5	[55]
V_2O_5	Nanobelt	20-30	Hydrothermal (autoclave)	Ethanol	200	3	[56]

Table 1.2 Literature papers focusing on nanoscale metal oxide semiconductor gas sensors.

However, there are several limitations to the development of the semiconducting nanowire gas sensors. First of all there is still a lack of systematic studies on structure/property relationships in nanowire gas sensors. Also, the sensing performance of nanowire semiconductor gas sensors has often been investigated while neglecting possible interferences from factors such as humidity; very few of the papers in Table 1.2 reported humidity responses. Finally, poor selectivity and insufficient long-term stability are major difficulties that nanowire semiconducting sensors need to overcome.

1.3.1.2 Synthesis of metal oxide semiconductor nanowires

Various chemical, physical, and electrochemical deposition techniques have been reported to create oriented MOS nanowires and nanorods. Methods such as catalytic growth via the

vapour-liquid-solid epitaxial (VSLE) mechanism, metal-organic chemical vapour deposition (MOCVD), pulsed laser deposition (PLD), chemical vapour deposition (CVD), hydrothermal synthesis, and electrodeposition have been particularly successful in creating highly oriented arrays of anisotropic nanowires of ZnO.[57] In general, there are two philosophically distinct approaches for creating nanowires: top-down and bottom-up strategies. The top-down approach usually including etching and lithography in bulk materials to form functional devices, this approach has been successful in many venues. In the bottom-up approach, functional nanostructures are assembled from well-defined chemically and/or physically synthesized building blocks.

Zinc oxide nanowires are commonly synthesized by a bottom-up approach.[58] CVD is a widely used route to produce high-purity, high-performance materials. In the CVD method, the precursor gases are first delivered into a reaction chamber at approximately ambient temperatures. In the reaction chamber a heated substrate or a wafer is used to expose to the volatile precursors, which react and decompose on the substrate surface to produce the desired solid phase. The by-products are removed by gas flow through the reaction chamber.[27] Commonly, CVD is a generic name for a group of processes that involve depositing a solid material from a gaseous phase. CVD processes include: atmospheric pressure CVD (APCVD), low-pressure CVD (LPCVD), vapour phase epitaxy (VPE),[59] chemical beam epitaxy (CBE),[60] and metal-organic chemical vapour deposition (MOCVD).[52]

Another promising method to synthesize Zinc oxide nanowires is physical vapour deposition (PVD. PVD is a technique quite similar to CVD, except that there is no chemical reaction happening during the deposition process. Variants of PVD include pulse laser deposition (PLD),[61] and sputter deposition. These methods can produce high-quality, single crystalline wires. However, these processes require elevated temperatures of 450 – 900 ℃ and often face other limitations of sample uniformly and substrate choice.[12,45]

Wang and co-workers have examined the synthesis, structure analysis,[62] and properties of nanoscale zinc oxide. They used solid-vapour thermal sublimation techniques to synthesize ZnO nanowires, nanobelts, nanorings, nanocages, and nanocombs. Zinc oxide nanowires and nanorods could be synthesized in many routes, such as vapour-liquid-solid (VLS) growth. In this technique, a metal catalyst, such as Au or Sn, was chosen and serves as the site for adsorbing the

incoming molecules (Zn complexes). A liquid alloy droplet composed of the metal catalyst is formed, followed by addition of the gaseous precursor to form an AuZn alloy. The metal liquid droplet serves as a preferential site for absorption of gas-phase reactant. Nanowire growth begins after the liquid becomes supersaturated in reactant materials and continues as long as the catalyst alloy remains in a liquid state and the reactant is available. The growth terminates when the temperature is below the eutectic temperature of the catalyst alloy or the reactant is no longer available. As a result, the nanowires obtained from the VLS process typically have a solid catalyst nanoparticle at the ends with sizes comparable to diameters of the connected nanowires.[63] The size of ZnO nanowires could be varied in wide range from several nanometers to thousands of nanometers by this technique. Nanobelts, which are ultra long ribbon-like structures, were first synthesized in 2001.[64] The typical widths of ZnO nanobelts were 30 to 300 nanometers, the width-to-thickness ratio was 5 to 10, and lengths were up to a few millimeters. Other than their interesting optical, electrical, semiconducting properties, zinc oxide nanobelts also showed interesting piezoelectric properties due to their atomic scale polarization,[65] and thus such nanobelts can be used as ZnO nanogenerators to convert mechanical energy into electric energy.[25] ZnO nanorings are circular shaped nanobelts; they are made of a ribbon bent evenly with a large radius and thickness of only ~ 10 nm. Nanocages are the hollow porous ZnO nanoparticles ranging in size from 10 to over 150 nm.[66] The mesoporous structures of nanocages make it a candidate for drug delivery use. Nanocombs are the comb-like nanobelts which have uniform and dense nanotips along one side of the comb ribbon.[67] This disc cap structure can be used to make nanoelectrodes for biosensor studies. Zinc oxide with other components such as doped ZnO nanobelts and ZnO core-shell nanowires and nanotubes are promising candidates for micro-sensors.[57]

In contrast to gas-phase technologies, solution approaches are appealing because of the low growth temperature (< 350 ℃), potential for scaling up, and straight-forward methods of producing high-density arrays. Hydrothermal syntheses are another convenient method to synthesis semiconductor nanowires. For example ZnO nanowires can be obtained by the hydrolysis of zinc nitrate in water in the presence of an amine. The zinc(II) is solvated by water, and exists as several monomeric hydroxyl species, such as $Zn(OH)^{+}_{(aq)}$, $Zn(OH)_{2(aq)}$, $Zn(OH)_{3}^{-}{}_{(aq)}$, and $Zn(OH)_{4}^{2-}{}_{(aq)}$. The stability of these complexes is depending on the pH and temperature of the solution. Solid ZnO nuclei are formed by the dehydration of these hydroxyl species, shown in

eq 1.21. Additives to the solution mixture, often amines, have a strong effect on the morphology of the resulting crystal.[24,32,68-72] Dutta reviewed the area of synthesis of the one-dimensional ZnO nanostructures by hydrothermal routes,[73] and showed that various ZnO nanostructures could be synthesized including nanowires, nanorods and flower and cabbage-like nanostructures by this method. [73]

$$Zn(OH)_{2(aq)} \rightarrow ZnO_{(s)} + H_2O_{(aq)} \quad (1.21)$$

Finally, electrodeposition has three main attributes that make it a promising technique for fabrication of nanowires. First, it can be used to grow functional materials through complex 2D or 3D templates; second, it can be performed at temperatures near room temperature from water-based electrolyte solutions; and finally, it can be scaled down to the deposition of a few atoms as well as up to larger dimensions. Electrodeposition within anodic alumina membrane templates is a bottom-up synthesis route which has been used with a great deal of success by numerous groups to synthesize metal and semiconductor nanostructures.[74-80] In a typical synthesis, a piece of anodic aluminum oxide (AAO) membrane with highly ordered nanopores is used as growth template. The dimensions of the nanopores can be varied over a large length scale. The backside of the membrane is homogeneously coated by a conducting layer, such as silver or GaN.[76] An aqueous solution with a certain concentration of metal cations is applied as the electrolyte, and the conducting layer acts as the cathode lead. In the electrodeposition process, the metal ions are reduced and the metal nanowires grow in the pores of the template. Meanwhile, a pure metal wire is used as the anode; during the electrodeposition process, the sacrificial anode is oxidized and therefore compensates the loss of metal cations in the electrolyte. The length of the nanostructures can be controlled by adjusting the amount of metal deposited. After the electrodeposition process, free-standing nanowires can be obtained through the removal of conducting layer and the dissolution of alumina membrane, as shown in Figure 1.9. Cao reviewed the growth of nanostructures using membranes as templates by using electrodeposition methods, metallic nanowires, such as Ni and Bi, conducting polymers, such as polyaniline (PANI), and oxides, such as ZnO, could be successfully synthesized with high efficiency.[81] Natan and coworkers described the synthesis of nanobarcodes also by electrodeposition routes using two or more electrodeposition routes.[82]

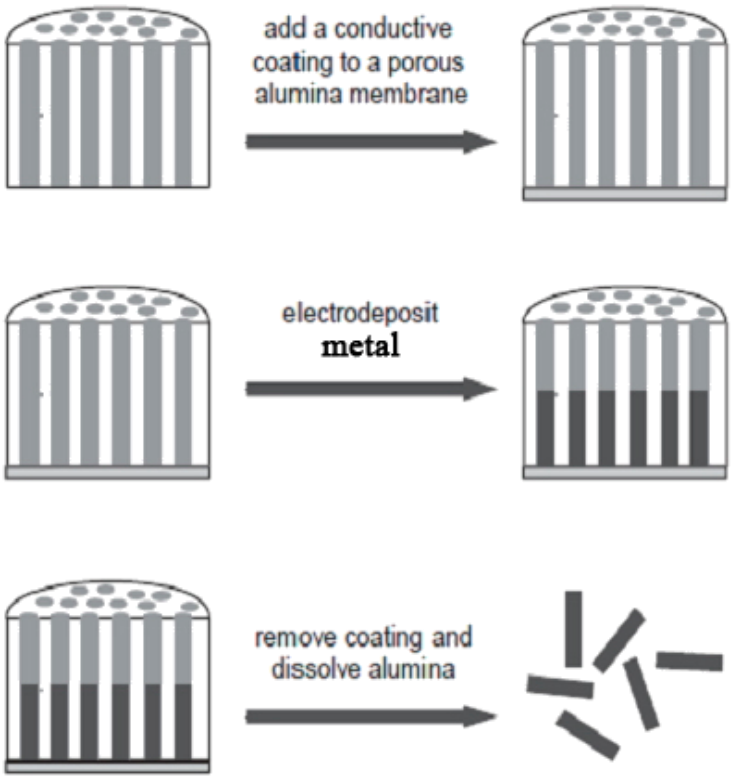

Figure 1.9 Schematic description of the template synthesis technique.[83] (Adapted with permission from reference 83. Copyright 2005 ACS.)

1.3.2 Metal-doped metal oxide semiconductor gas sensors

Another method to improve sensitivity and selectivity towards specific gases can be gained by adding small amounts of dopants into the pure MOS sensors. Many studies on the sensing properties of transition metal doped MOS sensors have been documented. The basic understanding behind the theories of additives on sensor performance was reviewed by Yamazoe.[84] Additives can play three distinct roles that can affect the gas response of MOS gas sensor. The first and the most basic role an additive can play is to control the grain size of the metal oxide semiconductor, which plays the key role in the sensitivity of the sensor. The second role is that the dopant can vary the thickness of the space-charge layer. For example, when antimony is substituted into a zinc oxide lattice, this results in an increase in conductivity. Thus, the space-charge thickness is shortened as more electrons are available at the surface to trap oxygen. In contrast, a substitution of aluminum into the lattice decreases the number of electrons

available at the surface which leads to a much thicker space-charge layer. Thus for aluminum-doped materials, changes in the thickness of the space-charge layer are directly related to the sensitivity of the oxide sensor to a reducing gas as the potential barriers between grains are much larger than those of the undoped oxide.

Finally, metal dopants can have a promotion effect on the response of an oxide substrate.[84] This is a common mechanism for a number of noble metal dopants. Typically the metal dopant acts as a catalyst for the catalytic oxidation of the reducing gas, lowering the activation energy and temperature at which the gas reacts with the oxide surface to a give a sensor response. The drop in sensor temperature is often accompanied by a drastic increase in the sensitivity towards certain gases. The low sensing temperature allows for the fabrication of low-power sensors which can operate at room temperature.

1.3.3 Carbon nanotube-based gas sensors

Carbon nanotubes (CNTs) had attracted a great deal of attention since their discovery by Iijima in 1991,[85] and have various potential applications, such as in composite materials and nanoelectronics.[85] CNTs have huge active surface areas, and the nanotubes are highly sensitive to very small external perturbations. These two characteristics make CNTs good candidates for nanoscale gas sensors. In 2000, Collins reported that CNTs are extremely sensitive to their chemical environment;[86] since then a number of groups have studied the sensing property of CNTs. This area has been well reviewed by Goldoni[87] shown that CNT sensors based on single-wall and Zhao reviewed that multi-wall CNTs and pure and metal-doped CNTs are able to detect a wide range of hazardous chemicals such as NO_2, NH_3, SO_2, NO, H_2, CO, etc. [88]

1.4 Knowledge Gap

Much research has been focused on the fabrication of nanoscale MOS materials for gas sensors, however, there are several major knowledge gaps in this field. First is the lack of systematic studies on the effect of the diameter of the nanowire sensor, which is considered a key point for creating highly sensitive MOS sensors. Meanwhile, the length of the MOS nanostructures is also an essential factor on the sensing properties, which has not been studied in

the previous work. Moreover, very few investigations report on the response of nanoscale MOS materials to water vapour. Given that the MOS gas sensors are usually sensitive to moisture, the detection of the target gas(es) can be difficult in high humidity environments. These points have all been studied in my project, and will be discussed in the subsequent section.

1.5 Research Objectives

We chose a systematic study on ZnO nanowire as gas sensors for this research project. The following three objectives were chosen:

1. A electrodeposition route using a template method is utilized to synthesize ZnO nanowires with different diameters, allowing a systematic study of the effect of nanowire diameter on sensing properties.

2. A hydrothermal route is employed in order to obtain nanostructures with variable lengths.

3. The sensing performance of the synthetic ZnO nanowires is characterized with three analyte gases: saturated water vapour (16000 ppm) in air, saturated EtOH vapour (35000 ppm) in air, and carbon monoxide in air.

1.6 References

(1) Kang, Z. C. *Functional Oxide nanocrystals*; Tsinghua University Press: Beijing, 2002.

(2) Berna, A. *Sensors* **2010**, *10*, 3882-3910.

(3) Bergman, I. *Anal. Proc.* **1986** *23*, 274-275.

(4) Weppner, W. *Sens. Actuators* **1987** *12*, 107-119.

(5) Bright, V. M.; Kolesar, E. S.; Hauschild, N. T. In *National Aerospace and Electronics Conferenc*; Proc. IEEE: 1994; Vol. 1, p 342-349.

(6) Seiyama, T.; Kato, A.; Fujiishi, K.; Nagatani, M. *Anal. Chem.* **1962**, *34*, 1502-1503.

(7) Hooker, S. A. In *The Nanoparticles 2002 Conference* 2002, p 1-7.

(8) Gong, H.; J. Q. Hua; Wang, J. H.; Ong, C. H.; Zhu, F. R. *Sens. Actuators, B* **2006**, *115*, 247-251.

(9) Wan, Q.; Li, Q. H.; Chen, Y. J.; Wang, T. H.; He, X. L.; Li, J. P.; Lin, C. L. *Appl. Phys. Lett.* **2004**, *84*, 3654-3656.

(10) Yamazoe, N.; Sakai, G.; Shimanoe, K. *Catal. Surv. Asia* **2003**, *7*, 63-75.

(11) Rout, C. S.; Krishna, S. H.; Vivekchand, S. R. C.; Govindaraj, A.; Rao, C. N. R. *Chem. Phys. Lett.* **2006**, *418*, 586-590.

(12) Lieber, C. M.; Wang, Z. L. *MRS Bull.* **2007**, *32*, 99-108.

(13) Moseley, P. T. In *Adam Hilger Series on Sensors*; Tofield, B. C., Ed.; Taylor & Francis: Bristol, 1987.

(14) Kolmakov, A.; Zhang, Y.; Cheng, G.; Moskovits, M. *Adv. Mater.* **2003**, *15*, 997-1000.

(15) Williams, D. E. *Sens. Actuators, B* **1999**, *57*, 1-16.

(16) Kohl, D. *Sens. Actuators* **1989**, *18*, 71-113.

(17) Kolmakov, A.; Moskovits, M. *Annu. Rev. Mater. Res.* **2004**, *34*, 151-180.

(18) Chen, Z.; Lu, C. *Sen. Lett.* **2005**, *3*, 274-295.

(19) Zhang, Y.; Yu, K.; Jiang, D.; Zhu, Z.; Geng, H.; Luo, L. *Appl. Surf. Sci.* **2005**, *242*.

(20) Harrison, P. G.; Willett, M. J. *Nature* **1988**, *332*, 227-339.

(21) Razatos, G.; Luthi, R.; Kerrigan, S. *Forensic Sci. Int.* **2005**, *153*, 17-21.

(22) Rao, B. B. *Mater. Chem. Phys.* **2000**, *64*, 62-65.

(23) Cheong, H. W.; Lee, M. J. *J. Ceram. Process. Res.* **2006**, *7*, 183-191.

(24) Greene, L. E.; Yuhas, B. D.; Law, M.; Zitoun, D.; Yang, P. *Inorg. Chem.* **2006**, *45*, 7535-7543.

(25) Wang, Z. L. *Appl. Phys. A: Mater. Sci. Process.* **2007**, *88*, 7-15.

(26) Özgür, Ü.; Alivov, Y. I.; Liu, C.; Teke, A.; Reshchikov, M. A.; S. Doğan, V. A.; Cho, S. J.; Morko ̧d, H. *J. Appl. Phys.* **2005**, *98*, 041301-103.

(27) Wang, Z. L. *J. Phys. Condens. Matter* **2004**, *16*, 829-858.

(28) Look, D. C. *Mater. Sci. Eng., B* **2001**, *80*, 383-387.

(29) Pearton, S. J.; Norton, D. P.; Ip, K.; Heo, Y. W.; Steiner, T. *Superlattices Microstruct.* **2003**, *34*, 3-32.

(30) Pearton, S. J.; Norton, D. P.; Ip, K.; Heo, Y. W.; Steiner, T. *J. Vac. Sci. Technol., B* **2004**, *22*, 932-948.

(31) Pol, V. d.; M., F. C. *Am. Ceram. Soc. Bull.* **1990** *69*, 1959-1965.

(32) Wang, J. X.; Sun, X. W.; Yang, Y.; Huang, H.; Lee, Y. C.; Tan, O. K.; Vayssieres, L. *Nanotechnology* **2006**, *17*, 4995-4998.

(33) Cho, P. S.; Kim, K. W.; Lee, J. H. *J. Electroceram.* **2006**, *17*, 975-978.

(34) Mitra, P.; Chatterjee, A. P.; Maiti, H. S. *Mater. Lett.* **1998**, *35*, 33-38.

(35) Fan, Z.; Wang, D.; Chang, P. C.; Tseng, W. Y.; Lu, J. G. *Appl. Phys. Lett.* **2004**, *85*, 5923-5925.

(36) Bott, B.; Jones, T. A.; Mann, B. *Sens. Actuators* **1984**, *5*, 65-73.

(37) Nanto, H.; Minami, T.; Takata, S. *J. Appl. Phys.* **1986**, *60*, 482-484.

(38) Egashira, M.; Kanehara, N.; Shimizu, Y.; Iwanaga, H. *Sens. Actuators* **1989**, *18*, 349-360.

(39) Sberveglieri, G.; Nelli, P.; Groppelli, S. *Mater. Sci. Eng., B* **1990**, *7*, 63-68.

(40) Nanto, H.; Sokooshi, H.; Kawai, T. *Sens. Actuators, B* **1993**, *14*, 715-717.

(41) Paraguay, D. F.; Miki-Yoshida, M.; Morales, J.; Solis, J.; Estrada, L. W. *Thin Solid Films* **2000**, *373*, 137-140.

(42) Choi, J. D.; Choi, G. M. *Sens. Actuators, B* **2000**, *69*, 120-126.

(43) Mukhopadhyay, A. K.; Mitra, P.; Chattopadhyay, D.; Maiti, H. S. *J. Mater. Sci. Lett.* **1996**, *15*, 431-433.

(44) Korotcenkov, G.; Han, S. D.; Cho, B. K.; Brinzari, V. *Crit. Rev. Solid State Mater. Sci.* **2009**, *34*, 1-17.

(45) Xia, Y.; Yang, P.; Sun, Y.; Wu, Y.; Mayers, B.; Gates, B. *Adv. Mater.* **2003**, *15*, 353-389.

(46) Cui, Y.; Wei, Q.; Park, H.; Lieber, C. M. *Science* **2001**, *293*, 1289-1292.

(47) Wang, Y.; Jiang, X.; Xia, Y. *J. Am. Chem. Soc.* **2003**, *125*, 16176-16177.

(48) Law, M.; Kind, H.; Messer, B.; Kim, F.; Yang, P. *Angew. Chem. Int. Ed.* **2002**, *41*, 2405-2408.

(49) Lv, Y.; Guo, L.; Xua, H.; Chu, X. *Physica E* **2007**, *36*, 102-105.

(50) Xu, J.; Chen, Y.; Chen, D.; Shen, J. *Sens. Actuators, B* **2006**, *113*, 526-531.

(51) Xu, H.; Liu, X.; Cui, D.; Li, M.; Jiang, M. *Sens. Actuators, B* **2006**, *114*, 301-307.

(52) Chatterjee, A. P.; Mitra, P.; Mukhopadhyay, A. K. *J. Mater. Sci.* **1999**, *34*, 4225-4231.

(53) Cheng, X. L.; Zhao, H.; Huo, L. H.; Gao, S.; Zhao, J. G. *Sens. Actuators, B* **2004**, *102*, 248-252.

(54) Liao, L.; Lu, H. B.; Li, J. C.; He, H.; Wang, D. F.; Fu, D. J.; Liu, C.; Zhang, W. F. *J. Phys. Chem. C* **2007**, *111*, 1900-1903.

(55) Zhang, D.; Liu, Z.; Li, C.; Tang, T.; Liu, X.; Han, S.; Lei, B.; Zhou, C. *Nano Lett.* **2004**, *4*, 1919-1924.

(56) Liu, J.; Wang, X.; Peng, Q.; Li, Y. *Adv. Mater.* **2005**, *17*, 764-767.

(57) Wang, Z. L. *Annu. Rev. Phys. Chem.* **2004**, *55*, 159-196.

(58) Xiang, B.; Wang, P.; Zhang, X.; Dayeh, S. A.; Aplin, D. P. R.; Soci, C.; Yu, D.; Wang, D. *Nano Lett.* **2007**, *7*, 323-328.

(59) Xu, C. X.; Sun, X. W.; Dong, Z. L.; Yu, M. B.; My, T. D.; Zhang, X. H.; Chua, S. J.; White, T. J. *Nanotechnology* **2004**, *15*, 839-842.

(60) Ohgaki, T.; Ohashi, N.; Kakemoto, H.; Wada, S.; Adachi, Y.; Haneda, H.; Tsurumi, T. *J. Appl. Phys.* **2003**, *93*, 1961-1965.

(61) Sun, Y.; Fuge, G. M.; Fox, N. A.; Riley, D. J.; Ashfold, M. N. R. *Adv. Mater.* **2005**, *17*, 2477-2481.

(62) Ding, Y.; Wang, Z. L. *J. Phys. Chem. B* **2004**, *108*, 12280-12291.

(63) Ding, Y.; Gao, P. X.; Wang, Z. L. *J. Am. Chem. Soc.* **2004**, *126*, 2066-2072.

(64) Pan, Z. W.; Dai, Z. R.; Wang, Z. L. *Science* **2001**, *291*, 1947-1949.

(65) Wang, Z. L. *MRS Bull.* **2007**, *32*, 109-116.

(66) Gao, P. X.; Wang, Z. L. *J. Am. Chem. Soc.* **2003**, *125*, 11299-11305.

(67) Wang, Z. L.; Kong, X. Y.; Zuo, J. M. *Phys. Rev. Lett.* **2003**, *91*, 185502-4.

(68) Vayssieres, L. *Adv. Mater.* **2003**, *15*, 464-466.

(69) Sugunan, A.; C.Warad, H.; Boman, M.; Dutta, J. *J. Sol-Gel Sci. Techn.* **2006**, *39*, 49-56.

(70) Greene, L. E.; Law, M.; Tan, D. H.; Montano, M.; Goldberger, J.; Somorjai, G.; Yang, P. *Nano Lett.* **2005**, *5*, 1231-1236.

(71) Sun, Y.; Riley, D. J.; Ashfold, M. N. R. *J. Phys. Chem. B* **2006**, *110*, 15186-15192.

(72) Wang, X.; Li, Y. *Inorg. Chem.* **2006**, *45*, 7522-7534.

(73) Baruah, S.; Dutta, J. *Sci. Technol. Adv. Mater.* **2009**, *10*, 013001-18.

(74) Chu, S. Z.; Wada, K.; Inoue, S.; Isogai, M.; Yasumori, A. *Adv. Mater.* **2005**, *17*, 2115-2119.

(75) Illy, B.; Shollock, B. A.; MacManus-Driscoll, J. L.; Ryan, M. P. *Nanotechnology* **2005**, *16*, 320–324.

(76) Lincot, D. *Thin Solid Films* **2005**, *487*, 40-48.

(77) Schonenberger, C.; Zande, B. M. I. v. d.; Fokkink, L. G. J.; Henny, M.; Schmid, C.; Kruger, M.; Bachtold, A.; Huber, R.; Birk, H.; Staufer, U. *J. Phys. Chem. B* **1997**, *101*, 5497-5505.

(78) Tian, M. L.; Wang, J. G.; Kurtz, J.; Mallouk, T. E.; Chan, M. H. W. *Nano Lett.* **2003**, *3*, 919-923.

(79) Wang, J. G.; Tian, M. L.; Kumar, N.; Mallouk, T. E. *Nano Lett.* **2005**, *5*, 1247-1253.

(80) Wu, Y.; Livneh, T.; Zhang, Y. X.; Cheng, G.; Wang, J.; Tang, J.; Moskovits, M.; Stucky, G. D. *Nano Lett.* **2004**, *4*, 2337-2342.

(81) Cao, G.; Liu, D. *Adv. Colloid Interface Sci.* **2008**, *136*, 45-64.

(82) Nicewarner-Pena, S. R.; Freeman, R. G.; Reiss, B. D.; He, L.; Pena, D. J.; Walton, I. D.; Cromer, R.; Keating, C. D.; Natan, M. J. *Science* **2001**, *294*, 137-141.

(83) Bentley, A. K.; Farhoud, M.; Ellis, A. B.; Lisensky, G. C.; Nickel, A.-M. L.; Crone, W. C. *J. Chem. Educ.* **2005**, *82*, 765-768.

(84) Yamazoe, N.; Miura, N. *Chemical sensor technology*; Ed S. Yamauchi: Kodansha, Tokyo, 1992.

(85) Iijima, S. *Nature* **1991**, *354*, 56-58.

(86) Collins, P. G.; Bradley, K.; Ishigami, M.; Zettl, A. *Science* **2000**, *287*.

(87) Goldoni, A.; Petaccia, L.; Lizzit, S.; Larciprete, R. *J. Phys. Condens. Matter.* **2010**, *22*.

(88) Zhao, Q.; Nardelli, M. B.; Lu, W.; Bernholc, J. *Nano Lett.* **2005**, *5*, 847-851.

CHAPTER 2

SYNTHESIS AND CHARACTERIZATION OF ZINC OXIDE NANOWIRES

2.1 Electrodeposition Route

2.1.1 Electrochemical deposition of Zn nanowire arrays

The electrodeposition method is one of the most widely used methods to synthesize metallic nanostructures. Although the electrodeposition method can be used on an industrial scale, all of our work was performed at a regular laboratory scale. ZnO nanowires were synthesized by a two-step procedure; Zn nanowires were first fabricated via electrodeposition, then the Zn nanowires were oxidized at 550 ℃ and zinc oxide nanowires were then obtained. [1-4]

An aqueous electrolyte solution was prepared in a glass beaker by dissolving $ZnCl_2$ (98+%, Aldrich) in a 30 mL buffer solution, which has a pH value of 3.00 (VWR). The zinc cation concentration of the electrolyte solution was $[Zn^{2+}] = 5.0$ mM.[5] In addition, 0.1003 M KCl (GR, EMD) and 2% wt gelatin (0.5978 g, granular, ScholAR) were added to the solution as a supporting electrolyte and stabilizer. In order to get nanowires with well-controlled diameters, porous anodic aluminum oxide (AAO) membranes (Whatman) with highly ordered nanopores were used as a growing template. The AAO templates have an overall diameter of 25 mm, with 60 μm height, while the diameter of the nanopores was variable from 20 – 200 nm, specified by the manufacturer. In a typical synthesis, a layer of silver gel (colloidal silver in acetone base, EMS) is painted onto the backside of the AAO membrane, and served as the conducting cathode lead. A piece of bulk Zn wire (99.95+%, Alfa) served as the anode.

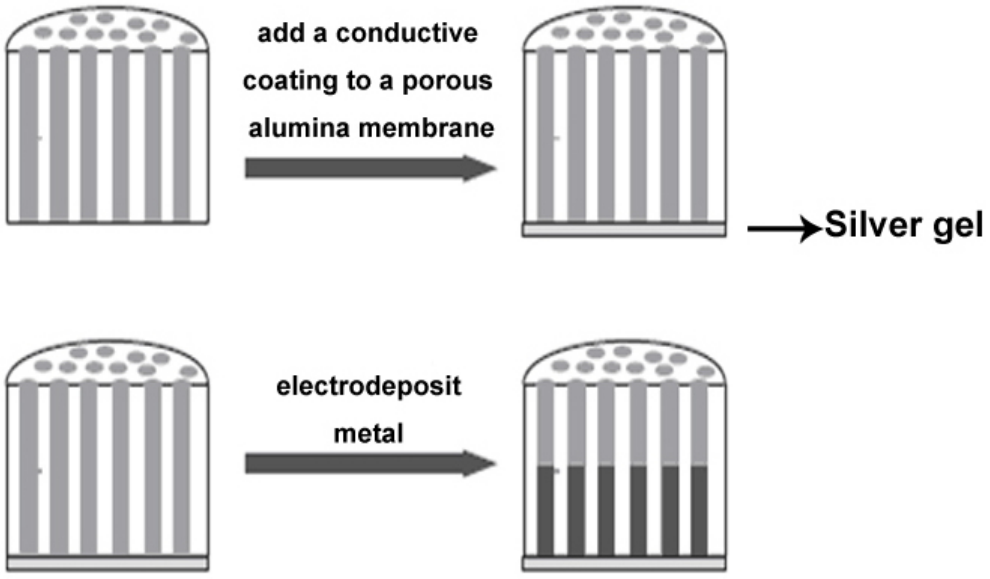

Figure 2.1 Schematic of electrodeposition strategy[6]. (Adapted with permission from reference 6. Copyright 2005 ACS.)

Before electrodeposition, the AAO template was impregnated by the electrolyte solution and ultrasonicated to remove any trapped gas inside the pores. Electrodeposition was carried out in a custom-made plastic cell (Figure 2.2) with the template backside (silver layer) facing downwards and connected to the cathode of the DC power-supply (Solartron SI1287/SI1260). The electrodeposition was carried out under galvanostatic conditions with a 1 mA current for 8 hours. Zn^{2+} is reduced at the cathode (eq 2.1), and deposited on the silver layer. The Zn nanowires array grew within the pores of the AAO membrane; Zn was oxidized at the anode during the electrodeposition to replenish the Zn^{2+} cations (eq 2.2). The typical voltage of electrodeposition was + 0.07 V (vs. NHE). The total amount of the Zn electrodeposited could be calculated as a function of charge. A typical voltage/time plot of the electrodeposition process is shown in Figure 2.3. The sharp voltage peak of the first stage which is likely due to the non-Faradaic current which is believed to be a diffusion controlled process, usually involves the formation and charging of the electric double layer on the electrode surface. Following this, the Faradaic current in stage 2 is due to the Zn nanowires deposition and growth within the template nanopores. Finally, when the template nanopores are all filled with the Zn nanowires, the Zn starts depositing on the surface of the AAO membrane, resulting in a lower voltage as shown in

stage 3. The growth process of Zn nanowires in the nanopores could also be monitored by the surface colour change of the AAO membrane; when the template nanopores were filled by the Zn nanowires and Zn began depositing on the top surface of the AAO membrane a darkening of the membrane surface was seen. The extra Zn could be removed from the AAO membrane by applied 1.0 M HNO_3.

$$Zn^{2+}{}_{(aq)} + 2\,e^- \rightarrow Zn_{(s)} \qquad \textbf{cathode} \qquad (2.1)$$

$$Zn_{(s)} - 2\,e^- \rightarrow Zn^{2+}{}_{(aq)} \qquad \textbf{anode} \qquad (2.2)$$

Figure 2.2 Picture of set-up of electrodeposition.

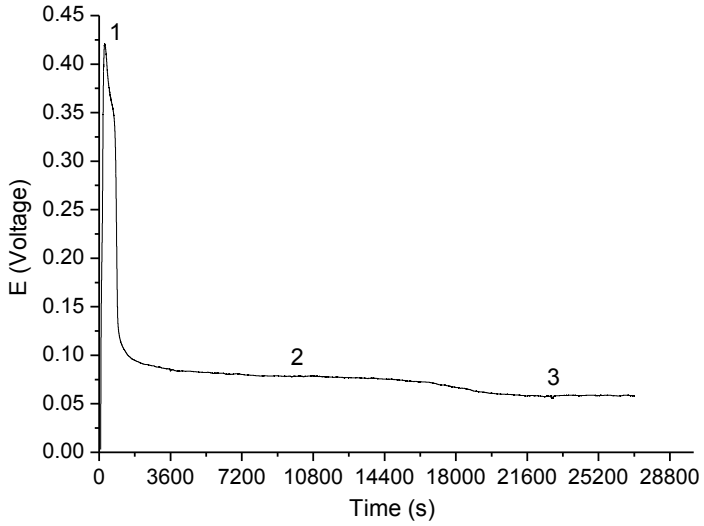

Figure 2.3 Typical voltage/time plot for the electrodeposition of Zn nanowires in an AAO template with 200 nm pores.

The synthetic Zn nanowire array within the nanopores of the template was annealed at 550 ℃ under a flow of air in a regular laboratory furnace (Lindberg/Blue M tube furnace) for 5 h. The Zn nanowires were oxidized into ZnO nanowires, as shown in equation 2.3. Powder X-ray diffraction confirmed the formation of ZnO, as detailed in section 2.1.2.3 below.

$$2\,Zn_{(s)} + O_2 \rightarrow 2\,ZnO_{(s)} \qquad (2.3)$$

After calcination of the AAO membrane template, the conducting Ag layer was physically removed from the AAO template by a sharp blade. The synthetic ZnO nanowires were separated from the AAO template by dissolving the template in a 0.75M KOH aqueous solution for 19 min. Both the Al_2O_3 template and ZnO nanowires are amphoteric oxides, which dissolve in both strong acids and bases. The ZnO nanowires were not released completely from the Al_2O_3 template in shorter KOH exposure times as the template was not totally dissolved, while with longer exposure times the synthetic ZnO nanowires were partially corroded. The template-free ZnO nanowires were then washed with distilled water several times, followed by separation from

the solution by means of centrifugation at 2500 rps. The freestanding nanowires were stored as a suspension in acetone until they were needed.

The ZnO nanowires were grown inside of the nanopores of the AAO templates. Thus the size and shape of the nanopores restricts the size and shape of the final product. Templates with different sizes of pores allowed us to adjust the shape and the size of the nanowires. Three highly ordered nanoporous AAO templates having pore diameters of d_N = 20, 100 and 200 nm (diameters specified by the manufacturer) were used in this experiment. In addition, by controlling the electrodeposition time, variation of the lengths of the nanowires could be obtained. In this work, all the ZnO nanowires were fabricated with lengths matched the length of the AAO template, which is 60 μm as specific by the manufacturer, thus the sensing properties of the ZnO nanowires could be investigated solely as the function of their diameters.

2.1.2 Characterization

The electrodeposited ZnO nanowires were characterized via optical microscopy, scanning electron microscopy, energy dispersive spectroscopy and X-ray diffraction.

2.1.2.1 Optical microscopy

The dimension of the synthetic ZnO nanowires was first characterized by an optical microscope (Nikon ME600) (resolution 200 nm). To prepare samples for optical microscopy, the acetone solution that contained the dispersed ZnO nanowires was added dropwise onto a glass substrate, followed by drying in air. The optical microscopy images of ZnO nanowires in Figure 2.4 show that ZnO nanowires were synthesized by the electrodeposition with a good yield of nanowires and little bulk ZnO powder. The average diameter of the synthetic ZnO nanowires is around 270 nm. However, some ZnO nanowires broke into small pieces during the extraction and separation process, as can be seen in Figure 2.4 (a).

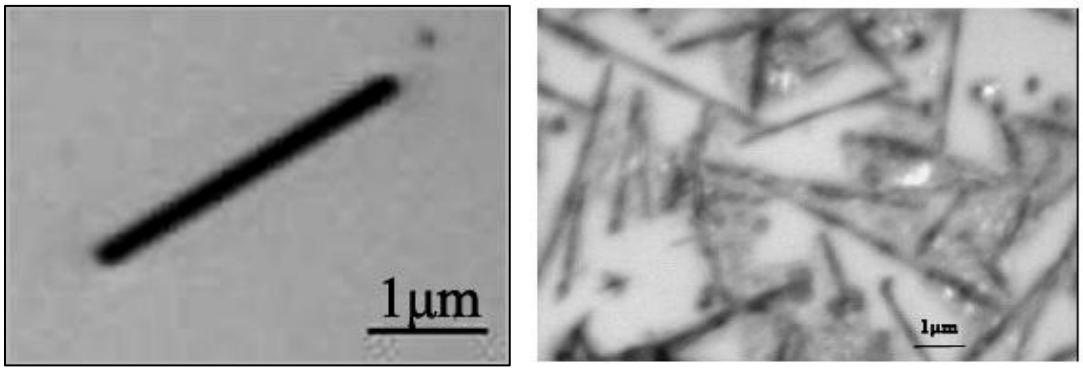

(a) (b)

Figure 2.4 Optical microscopy images of ZnO nanowires with an average diameter about 270 nm synthesized in a 200 nm AAO template. (a) One single broken ZnO nanowire. (b) ZnO nanowires.

2.1.2.2 Scanning electron microscopy

Further investigation on the dimension of the nanowires was carried out by scanning electron microscopy (SEM) (JEOL 840A & JEOL JSM-6360) to investigate the average diameter of the synthetic ZnO nanowires. A thin layer of Au was coated on the top of the samples in order to improve resolution and prevent charging. The SEM images for nanowires synthesized in different AAO templates are shown in Figure 2.5. Three AAO membranes with different sized nanopores were used as the synthesis templates, in order to obtain nanowires with variable diameters. The ZnO nanowires shown in Figure 2.5 (a), grown in AAO templates with nanopores of 20 nm, have an average diameter of 30 $\pm$ 3 nm. The second batch of nanowires synthesized in the AAO templates with nanopores of 100 nm have an average size of 150 $\pm$ 12 nm (Figure 2.5 (b)), while the average diameter of the third batch of nanowires grown in the AAO templates with 200 nm nanopores was observed to be 280 $\pm$ 30 nm. The average diameter and the size distribution of each batch of nanowires were calculated based on 20-30 nanowires counted. Data are listed in Table 2.1. The SEM images show that the synthetic ZnO nanowires have diameters significantly larger than the average diameter of the pores of their templates. As the ionic radius of Zn is 0.074 nm and for O is around 0.14 nm, this size expansion could be due to the expansion of the Zn nanowires upon oxidation to ZnO. In addition, the pore sizes of the

AAO templates reported by supplier refer to the ability to completely filter objects of that size, and are not necessarily the average pore size. Although the AAO membranes have a thickness of 60 μm, the SEM images show that the length of our nanowires is on average about 10 ± 2 μm, this might be due to corrosion by the KOH when the ZnO nanowires were released from the template pores.

Diameter of ZnO nanowires	**Diameter of AAO template nanopores (manufacturer data)**
31 ± 3 nm	20 nm
150 ± 12 nm	100 nm
280 ± 30 nm	200 nm

Table 2.1 Diameters of ZnO nanowires and the pore diameters of their respective AAO templates.

The composition of the nanowires was investigated by energy dispersive spectroscopy (EDS) (Oxford Instruments). An EDS map of a ZnO nanowire with 300 nm diameter is shown in Figure 2.6. The major components of the nanowires are zinc and oxygen. The small amount of carbon is likely coming from the carbon tape used to attach the sample onto the specimen holder and significantly, no alumina contamination is seen.

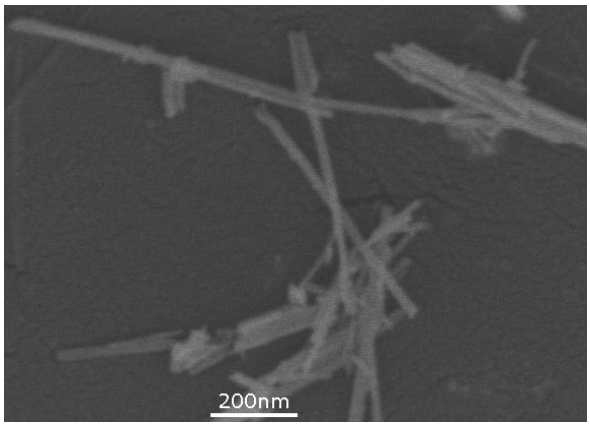

(a)

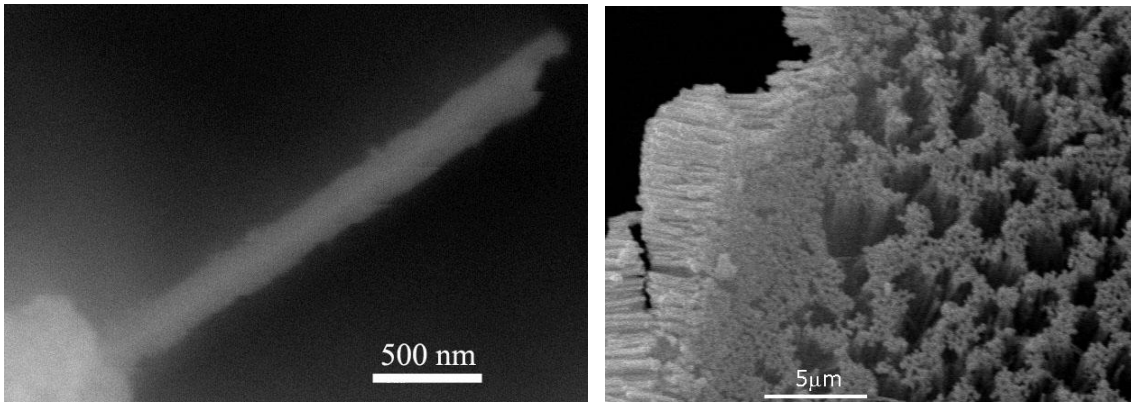

(b)

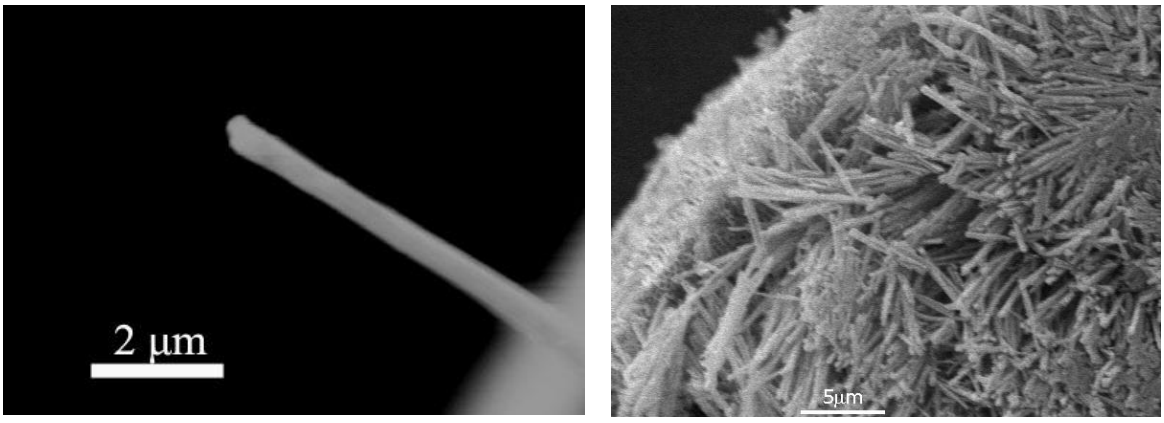

(c)

Figure 2.5 SEM images of ZnO nanowires synthesized by electrodeposition in AAO templates. ZnO nanowires with a diameter of: (a) 31 ± 3 nm; (b) 150 ± 12 nm; (c) 280 ± 30 nm.

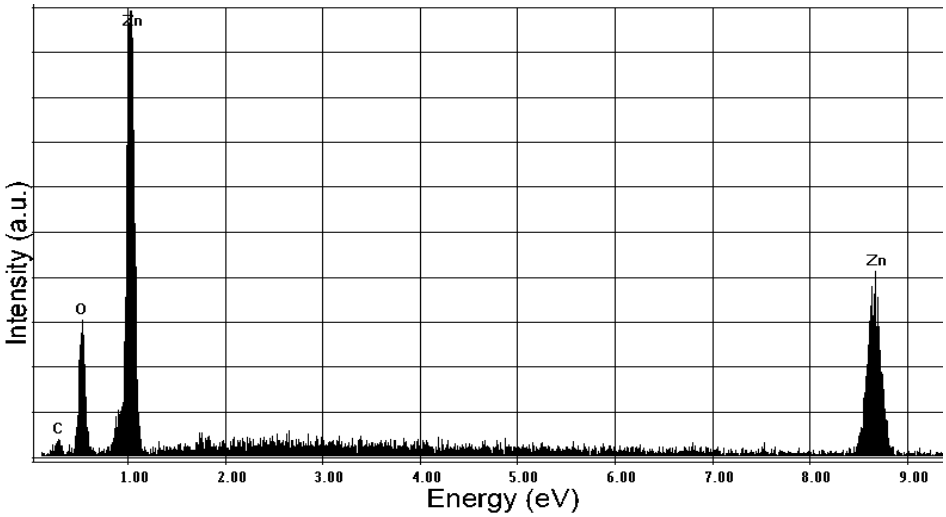

Figure 2.6 EDS spectrum of ZnO nanowires synthesized by electrodeposition.

2.1.2.3 X-ray diffraction

The crystallographic structure of the synthetic ZnO nanowires was characterized by powder X-ray diffraction (Rigaku Rotaflex RU-200 rotating anode XRD) with a Cu source and 2θ range of 30 - 70 º. Figure 2.7 shows the pXRD pattern of the ZnO nanowires synthesized in the AAO templates that had nanopores of 20 nm diameter. The XRD pattern shows that all the peaks can be indexed to hexagonal wurtzite ZnO (JCPDS card No. 79-2205). The domain size of the crystal can be estimated from the full width at half maximum (FWHM) of the peaks by means of the Scherrer formula,[5]

$$D = \frac{K\lambda}{b\cos\theta} \qquad (2.4),$$

where λ is the wavelength of the incident beam (1.7889 Å); b is the corrected FWHM of the peak in radians (2 θ); θ is the diffraction angle, and K is Scherrer constant, usually assumed to be 1. The average crystallite size calculated from (110) peaks was approximately 33 ± 3 nm.

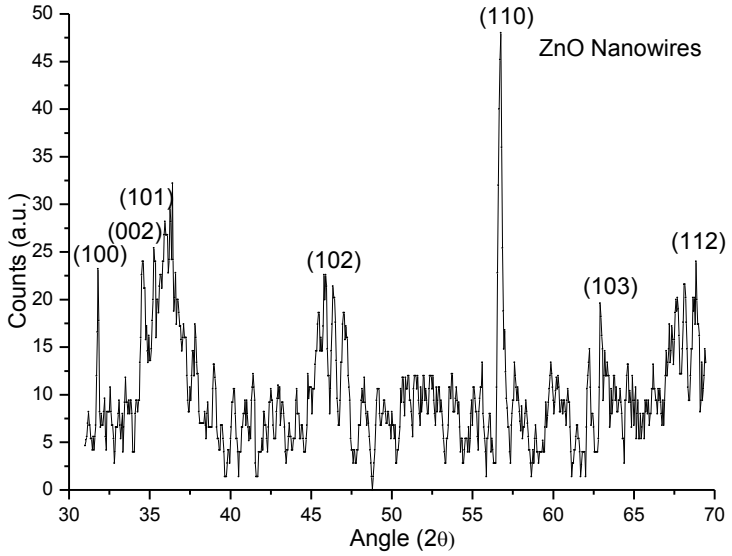

Fig 2.7 Powder XRD pattern of ZnO nanowires synthesized from a 20 nm AAO template. Some amorphous material in the sample resulted in the broad peaks at 36 and 47 degrees.

2.2 Hydrothermal Route

2.2.1 Synthesis process

The hydrothermal route is another convenient method to synthesize ZnO nanostructures.[7] ZnO nanorods can be synthesized under hydrothermal conditions at low temperature and low cost.[8-10] In order to get well-defined ZnO nanowires, a seed solution of suspended small ZnO nanocrystals was first prepared in 2-propanol.[10-15] 0.2000 g of zinc acetate dihydrate ($Zn(CH_3CO_2)_2 \bullet 2H_2O$) (98+%, Alfa) was dissolved in 20 mL of 2-propanol (99.7+%, Alfa) under vigorous stirring at 50 ℃ and subsequently diluted to a total volume of 200 mL followed by chilling to 0 ℃. 20 mL of a 0.10 M NaOH solution in 2-propanol was then added to the $Zn(CH_3CO_2)_2$ solution at 0 ℃ within 1 min under constant stirring. The liquid was then immersed in a preheated water bath at 65 ℃ for 15 min., followed by the addition of 5.23 g of PVP (poly(vinylpyrrolidone)) (Alfa) under constant stirring. The solution was then heated for 2 h at 55 ℃. The final solution was a light yellow color, and was found to consist of ZnO nanoparticles as detailed in section 2.2.2.1.

Si/SiO_2 wafers were used as a growing template in the hydrothermal route to synthesize ZnO nanorods.[16] The wafer was cut into 1 cm x 1 cm pieces by a diamond knife, followed by the addition 10 drops of the ZnO crystal seed solution dropwise onto the wafer, which was then dried in air. The wafer was then calcined at 550 ℃ in air for 5 h in order to remove the organic polymer coating.

The ZnO growth solution was prepared by mixing a 10 mL sample of 2.0 mM HMTA (hexamethylenetetramine) (99%, Aldrich) aqueous solution with a 10 mL sample of 2.0 mM $Zn(NO_3)_2$ (98%, Aldrich) under constant stirring in a regular laboratory vial.[12,17] The silica wafer with ZnO seeds was placed in the growth vial, and the vial was then immersed into a preheated oil bath at 95 ℃ for 8 hours. White ZnO nanorods grew on the Si wafer; following the chemistry as shown in eq 2.5 - 2.8. The $[Zn(C_6H_{12}N_4H_4)_n]^{(4n-2)-}{}_{(aq)}$ salts are the precursor for both the Zn(II) and OH^- species; the HMTA cation decomposes *in-situ* to form the OH^- anions. The overall reaction is shown in eq 2.9.[18] After cooling, the ZnO nanorods were washed with deionized water several times, and then dried in air. The structure of hexamethylenetramine ($C_6H_{12}N_4$) is shown in Figure 2.8.

$$C_6H_{12}N_{4(aq)} + H_2O_{(l)} \rightarrow C_6H_{12}N_4H_4{}^{4+} + 4OH^-{}_{(aq)} \quad (2.5)$$

$$C_6H_{12}N_4H_4{}^+{}_{(aq)} + Zn(NO_3)_{2(aq)} \rightarrow [Zn(C_6H_{12}N_4H_4)_n]^{(4n+2)+}{}_{(aq)} + 2\ NO_3{}^-{}_{(aq)} \quad (2.6)$$

$$[Zn(C_6H_{12}N_4H_4)_n]^{(4n+2)+}{}_{(aq)} + 6\ H_2O_{(l)} \rightarrow Zn^{2+}{}_{(aq)} + 6\ HCHO_{(aq)} + 4\ NH_4^+{}_{(aq)} + 6\ OH^-{}_{(aq)} \quad (2.7)$$

$$Zn^{2+}{}_{(aq)} + 2\ OH^-{}_{(aq)} \rightarrow Zn(OH)_{2(aq)} \rightarrow ZnO_{(s)} + H_2O_{(l)} \quad (2.8)$$

$$C_6H_{12}N_{4(aq)} + 8\ H_2O_{(l)} + 2\ Zn^{2+}{}_{(aq)} \rightarrow 6\ HCHO_{(aq)} + 4\ NH_4^+{}_{(aq)} + 2\ ZnO_{(s)} \quad (2.9)$$

The ZnO nanorods were grown from the ZnO crystal seeds.[19,20] The size and the density of the ZnO crystal seeds have a crucial effect on the dimensions of the final ZnO nanorods; smaller crystal seeds should result into thinner nanorods, while a lower density of the seeds should lead to longer nanowires being formed.[21,22]

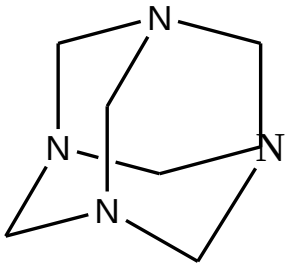

Figure 2.8 Structure of hexamethylenetramine.

2.2.2 Characterization

2.2.2.1 ZnO nanoparticle seeds

The average size of the ZnO nanoparticle seeds was determined by UV-Vis spectroscopy. From the UV-Vis spectra in Figure 2.9, the cross point of the tangent on the curve and axis shows the band gap which is 365 nm, or 3.41 eV. Using eq 2.11 as shown below, the grain size of the synthetic ZnO nanoparticles seeds was calculated to be 1.8 ± 0.2 nm,[16]

$$eE^* = eE_g^{bulk} + \frac{h^2\pi^2}{2r^2}\left(\frac{1}{m_e^* m_0} + \frac{1}{m_h^* m_0}\right) - \frac{1.8e^2}{4\pi\varepsilon\varepsilon_0 r} - \frac{0.124e^4}{h^2(4\pi\varepsilon\varepsilon_0 r)^2}\left(\frac{1}{m_e^* m_0} + \frac{1}{m_h^* m_0}\right)^{-1} \quad (2.11),$$

where E_g^{bulk} is the bulk band gap (eV), which is 3.37 eV for bulk ZnO;[16] ħ is the Planck constant, r is the particle radius, m_e is the hole effective mass, m_0 is the free electron mass, e is the charge on the electron, ϵ is the relative permittivity, and ϵ_0 is the permittivity of free space.

Scanning electron microscopy (SEM) (JEOL 840A & JEOL JSM-6360) was applied to investigate the dimension and density of ZnO growth seeds dispersed on the wafer after calcination. A thin layer of Au was coated on the top of the samples in order to get better resolution and to prevent charging. A SEM image of the nanoparticle seeds is shown in Figure 2.10, from which, the average size of the ZnO seeds after calcination was measured as 136 ± 15 nm and the density of the ZnO seeds on the wafer is approximately 10/μm^2. The particle size of the ZnO seeds is much larger than as calculated for the as-synthesized seeds from their UV-Vis

spectra; this is likely due to the aggregation of the ZnO particles into larger ZnO clusters during the calcination process.

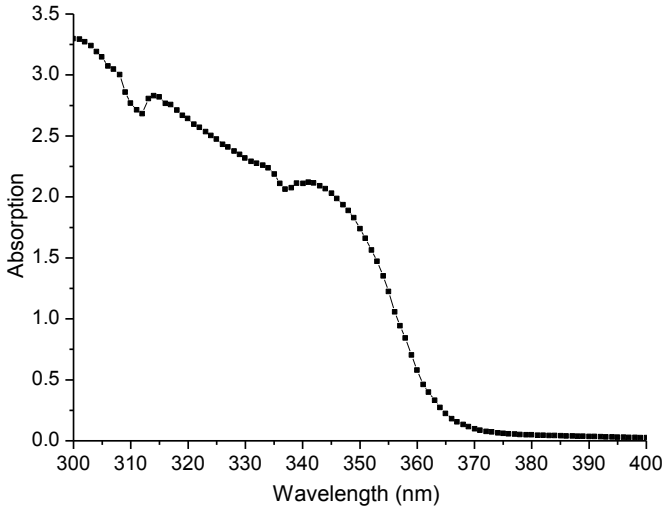

Figure 2.9 UV-Vis spectrum of ZnO nanoparticle seeds.

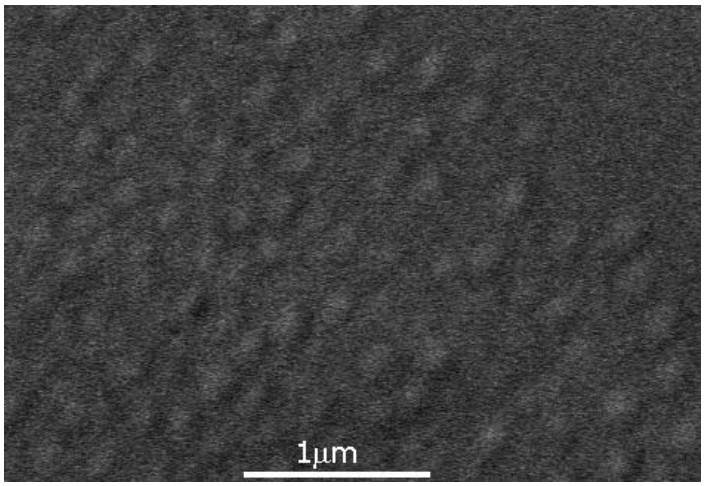

Figure 2.10 SEM image of ZnO seeds on a silica wafer.

2.2.2.2 ZnO nanorods

The dimensions of the nanorods grown by the hydrothermal synthesis were investigated by SEM. The SEM images in Figure 2.11 show that nanorods are synthesized by the hydrothermal route. The average dimensions of the nanorods were measured based on the images, the average diameter was 350 ±20 nm while the average length of the nanorods was 2.5 ±0.3 μm.

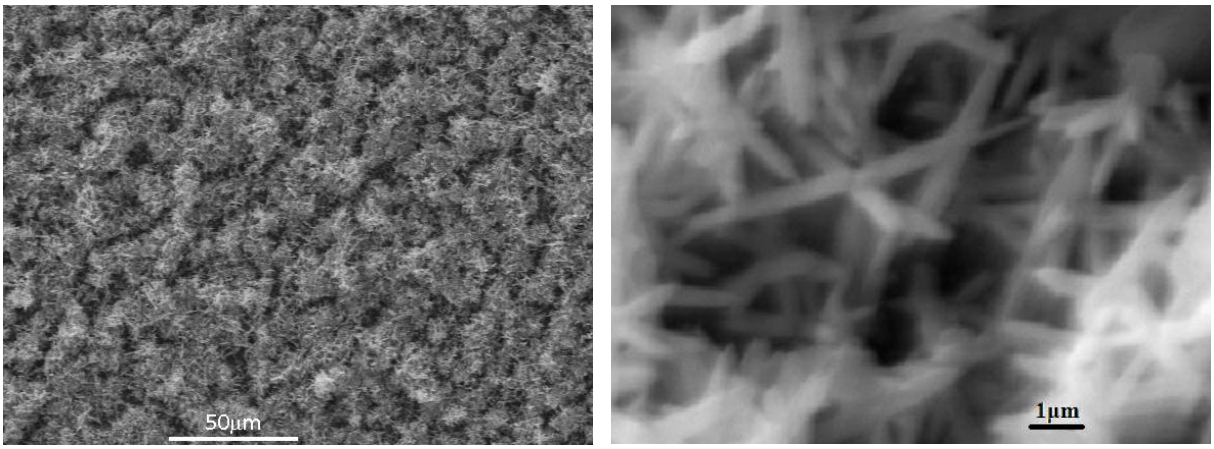

Figure 2.11 SEM images of ZnO nanorods synthesized by the hydrothermal route.

The composition of the ZnO nanorods was investigated by energy dispersive spectroscopy (EDS). An EDS spectrum is shown below in Figure 2.12. The major components of the ZnO nanorods, as expected, are zinc and oxygen. The ZnO nanorods were grown on a Si/SiO_2 wafer, hence the Si peak in the EDS spectra.

The crystal structure of ZnO nanorods synthesized by the hydrothermal route was investigated by powder XRD. Figure 2.13 shows the powder XRD pattern of the ZnO nanorods synthesized by hydrothermal route. All the peaks could be indexed to hexagonal wurtzite ZnO (JCPDS card No. 79-2205), which is similar with the ZnO nanowires synthesized by electrodeposition. The crystalline domain size of the nanorods could be calculated from the FWHM of the peaks (100) and (101) by means of the Scherrer formula, resulted in an average diameter about 360 nm.

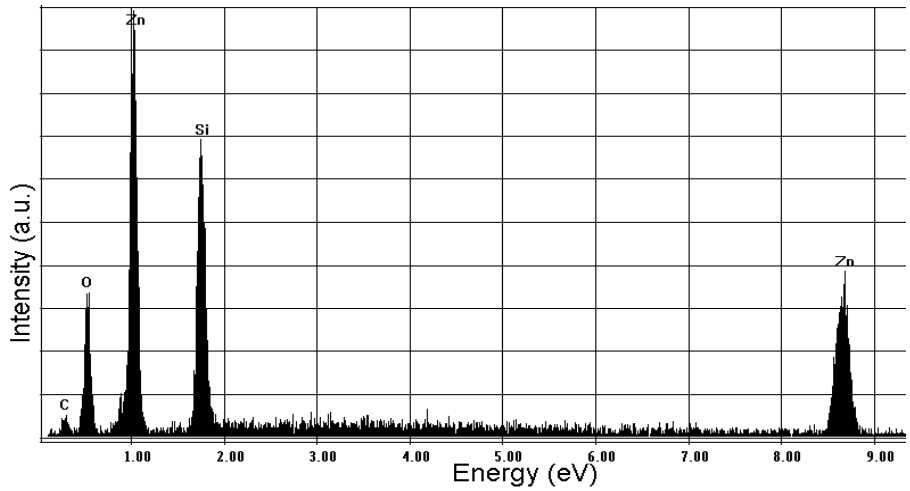

Figure 2.12 EDS spectrum of ZnO nanorods synthesized by the hydrothermal route.

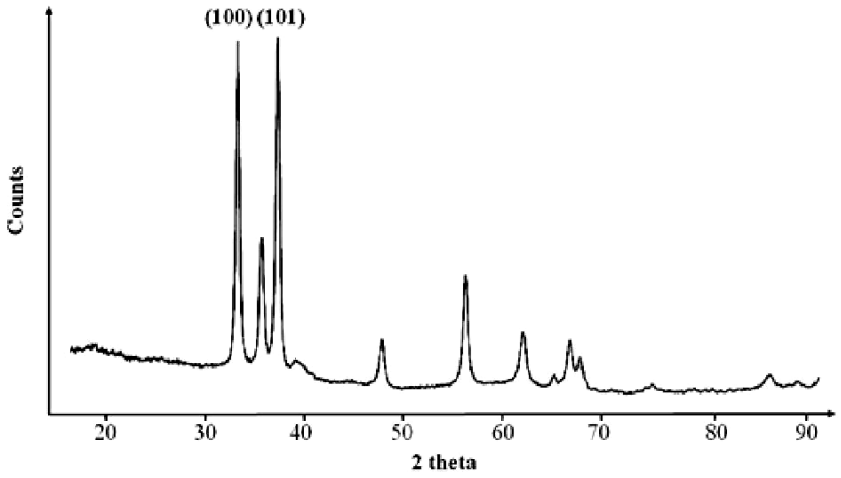

Figure 2.13 Powder XRD pattern of ZnO nanorods synthesized by the hydrothermal route.

2.3 References

(1) Özgür, Ü.; Alivov, Y. I.; Liu, C.; Teke, A.; Reshchikov, M. A.; S. Doğan, V. A.; Cho, S. J.; Morko ç, H. *J. Appl. Phys.* **2005**, *98*, 041301-103.

(2) Goux, A.; Pauport é, T.; Chivot, J.; Lincot, D. *Electrochim. Acta* **2005**, *50*, 2239-2248.

(3) Rao, B. B. *Mater. Chem. Phys.* **2000**, *64*, 62-65.

(4) Cheng, X. L.; Zhao, H.; Huo, L. H.; Gao, S.; Zhao, J. G. *Sens. Actuators, B* **2004**, *102*, 248-252.

(5) Hilber, T.; Letonja, P.; Marr, R.; Poit, P.; Siebenhofer, M. *Part. Part. Syst. Charact.* **2002**, *19*, 342-347.

(6) Bentley, A. K.; Farhoud, M.; Ellis, A. B.; Lisensky, G. C.; Nickel, A.-M. L.; Crone, W. C. *J. Chem. Educ.* **2005**, *82*, 765-768.

(7) Patterson, A. L. *Phys. Rev.* **1939**, *56*, 978-982.

(8) Vayssieres, L. *Adv. Mater.* **2003**, *15*, 464-466.

(9) Greene, L. E.; Yuhas, B. D.; Law, M.; Zitoun, D.; Yang, P. *Inorg. Chem.* **2006**, *45*, 7535-7543.

(10) Baruah, S.; Dutta, J. *Sci. Technol. Adv. Mater.* **2009**, *10*, 013001-18.

(11) Ma, X.; Zhang, H.; Ji, Y.; Xu, J.; Yang, D. *Mater. Lett.* **2005**, *59*, 3393-3397.

(12) Sun, Y.; Fuge, G. M.; Fox, N. A.; Riley, D. J.; Ashfold, M. N. R. *Adv. Mater.* **2005**, *17*, 2477-2481.

(13) Sugunan, A.; C.Warad, H.; Boman, M.; Dutta, J. *J. Sol-Gel Sci. Techn.* **2006**, *39*, 49-56.

(14) Ho, G. W.; Wong, A. S. W. *Appl. Phys. A* **2007**, *86*, 457-462.

(15) Greene, L. E.; Law, M.; Tan, D. H.; Montano, M.; Goldberger, J.; Somorjai, G.; Yang, P. *Nano Lett.* **2005**, *5*, 1231-1236.

(16) Wong, E. M.; Hoertz, P. G.; Liang, C. J.; Shi, B.-M.; Meyer, G. J.; Searson, P. C. *Langmuir* **2001**, *17*, 8362-8367.

(17) Greene, L. E.; Law, M.; Goldberger, J.; Kim, F.; Johnson, J. C.; Zhang, Y.; Saykally, R. J.; Yang, P. *Angew. Chem. Int. Ed.* **2003**, *42*, 3031-3034.

(18) Zhu, H.; Yang, D.; Zhang, H. *Inorg. Mater.* **2006**, *42*, 1210-1214.

(19) Cho, P. S.; Kim, K. W.; Lee, J. H. *J. Electroceram.* **2006**, *17*, 975-978.

(20) Song, J.; Lim, S. *J. Phys. Chem. C* **2007**, *111*, 596-600.

(21) Wang, J. X.; Sun, X. W.; Yang, Y.; Huang, H.; Lee, Y. C.; Tan, O. K.; Vayssieres, L. *Nanotechnology* **2006**, *17*, 4995-4998.

(22) Chatterjee, A. P.; Mitra, P.; Mukhopadhyay, A. K. *J. Mater. Sci.* **1999**, *34*, 4225-4231.

CHAPTER 3
ZINC OXIDE NANOWIRE GAS SENSORS

3.1 Experimental Protocols for Sensor Measurements

3.1.1 Experimental diagram of gas path

The sensing performance of the synthetic ZnO nanowire gas sensors was investigated towards three analyte gases; (1) saturated water vapour (16000 ppm) in air, (2) saturated ethanol vapour (35000 ppm) in air, and (3) 2000 ($\pm$ 5) ppm carbon monoxide in air. The diagram of the flow path is shown in Figure 3.1; two gas tanks served as the air source (Praxair) and analyte gas source of the experiments. Flow meters regulated the flow rates of the gases; the typical flow rates for the analyte gases and air were 675 mL/min and 1250 mL/min, respectively. The pressure of the analyte gases in the sensing chamber was kept constant.

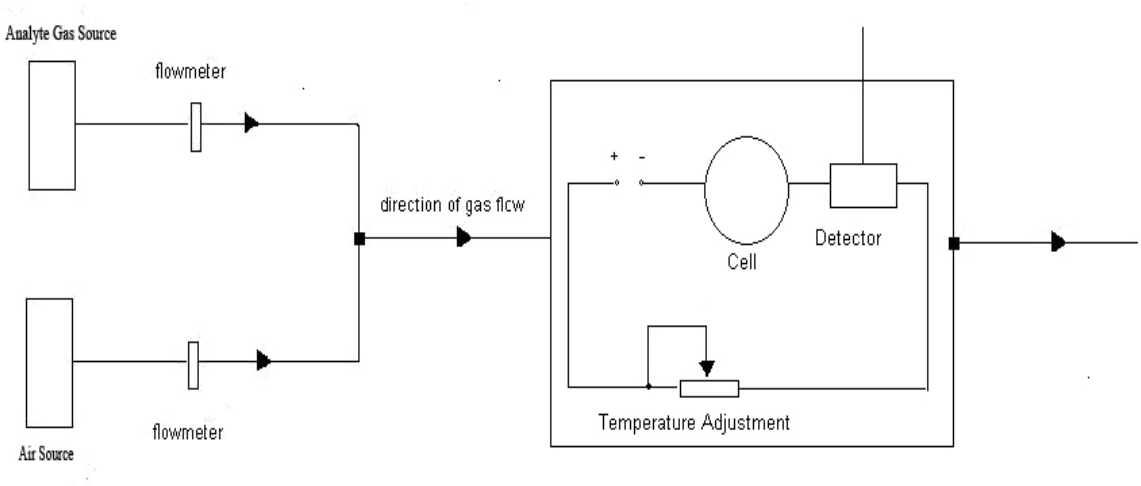

Figure 3.1 Chart of flow path used in the sensing experiments.

3.1.2 Microreactor

The sensor measurements were carried out in a customized microreactor chamber, which is shown in Figure 3.2. The microreactor chamber was made of stainless steel with a transparent acrylic cover with an O-ring to prevent leakage. The green electrical board which is located in the chamber allows for temperature control via a Wheatstone bridge (City Technology). Air and

analyte gases enter the chamber through inlet 1 and leave the chamber through outlet 2. The nanostructured ZnO powders were placed on the interdigitated electrode of microreactor 3 (which can be removed from the reactor). An external power supply is connected to the microreactor through supply 4 while the conductivity signal across the interdigitated array is measured via connection 5. The screw 6 allows adjustments to the temperature of the electrode via changing the voltage across a Wheatstone bridge.

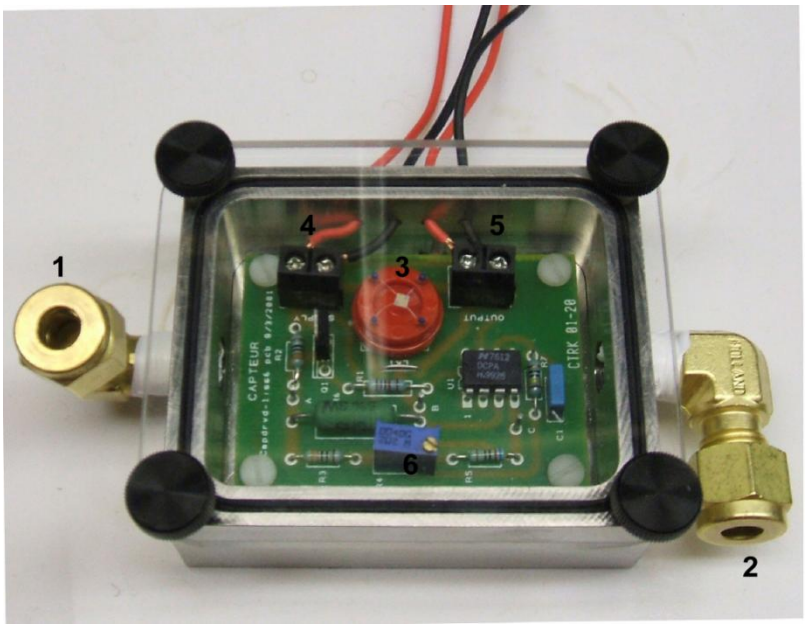

Figure 3.2 Picture of customized microreactor chamber used in sensing experiments.

3.1.3 Interdigitated electrode

One of the important variables on the sensing response of the conductometric sensors is the microstructure of the sensing electrode. The use of electrode microstructures can offer advantages of diffusion-controlled currents and low charging currents.[1,2] Many analyte gases, such as ethanol, easily decompose on metal oxide surfaces at elevated sensing temperatures, thus concentration gradients of the analyte gases are commonly observed through the metal oxide material, and the concentration of the analyte gas is much lower at the surface than in the external atmosphere. A shorter path of gas diffusion can lead to a higher concentration of analyte gas, resulting in a better sensitivity. Williams and co-workers fabricated electrodes with

interdigitated array microstructures in the 1970s.[1,2] The interdigitated array (IDA) electrodes, shown in Figure 3.3, are now commonly used electrode configurations for conductometric sensing applications. The sensor materials are dispersed onto the IDA electrode, and the actual sensing response is measured at the surface of the IDA electrode as the analyte gases diffuses through the sample to the sensor surface.

The effects of analyte gas diffusion on the sensitivity of the response are affected by the dispersion of the sensor material on the surface of IDA electrodes. If the material is randomly dispersed on the electrodes, there will be a lot of random macropores from the exterior to the surface of the electrode, and this will facilitate the diffusion of the analyte gases to the electrode. For powdered sensors, a small amount of an organic vehicle (in this case glycerol) is commonly mixed with the powder. The mixture is then homogenized by ball-milling or other techniques, and the resulting slurry is applied onto the IDA electrodes by screen-printing. The organic vehicle is then removed by calcination to give a reasonably well defined macroporous sensor film.[3]

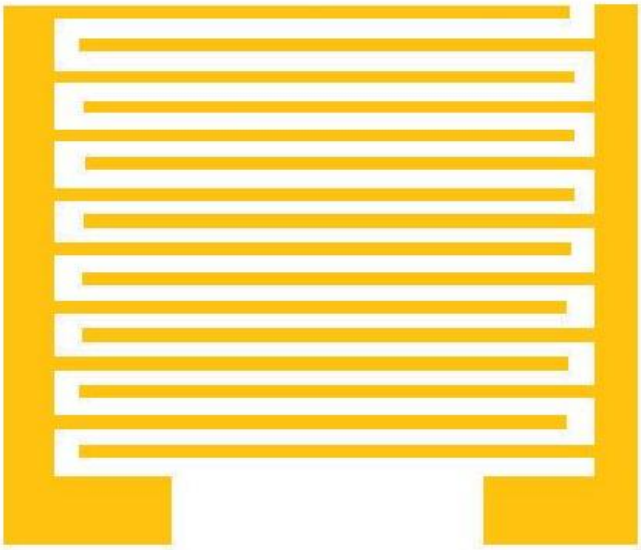

Figure 3.3 Microstructure of an interdigitated array electrode.

3.1.4 Gas sensor preparation

Our free-standing ZnO nanostructures were first mixed with a small amount of glycerol, which is used as an organic vehicle. The mixture was gently milled by an agate mortar, resulting in a homogenized ZnO paste. This mixture was then pasted onto the interdigitated array electrodes, followed by sintering at 550 ℃ for over 10 hours in air. After the glycerol was burned, the ZnO materials were left on the IDA electrodes.

The setup of our microreactor is shown in Figure 3.4. ZnO nanostructures were homogenously spread on the sensor surface, which consists of an alumina substrate with gold interdigitated array electrodes on the top and a meandering platinum resistor heater on the bottom. A DC power-supply with a fixed voltage of 6 V was utilized to operate the heater. The temperature is controlled by a Wheatstone bridge (City Technology) which allows for a constant temperature to be applied to the sensor of ±1 ℃. A fixed voltage of 10 mV, which is supplied by a DC power, is applied across the interdigitated array electrodes, and the output current is recorded.

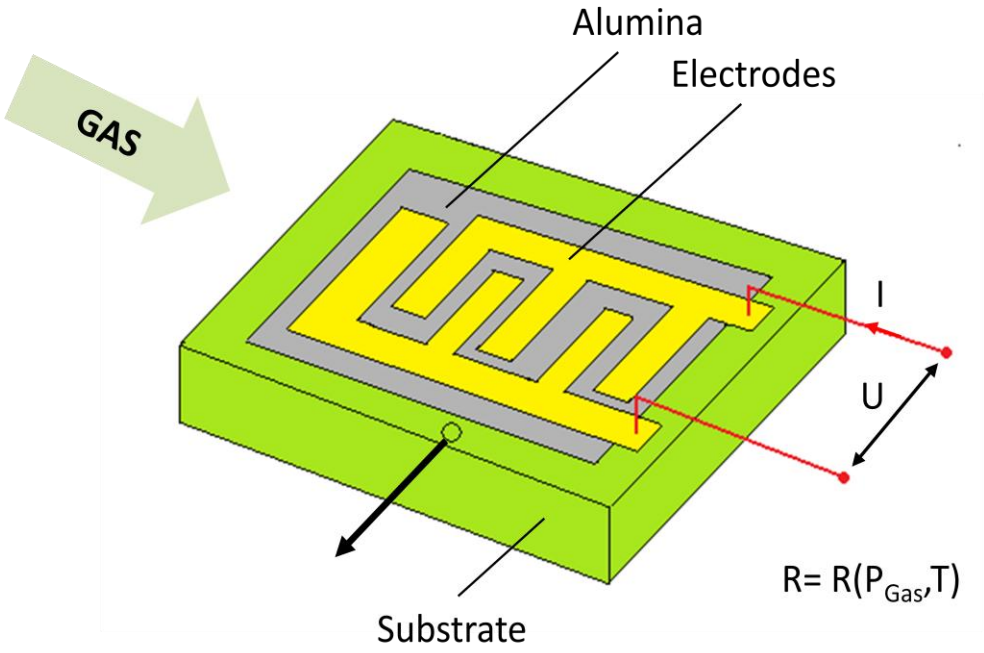

Figure 3.4 Set-up of microreactor with interdigitated array electrodes.

3.1.5 Typical diagram of gas sensing

The recorded current is inversely proportional to the resistance of the sensors which cover the electrode, **I = V / R**. Thus, the sensitivity of the sensor can be represented by eq 3.1,[4]

$$S_g = \frac{R_a}{R_g} = \frac{I_g}{I_a} \quad (3.1),$$

where I_g is the current when the sensor is exposed to the analyte gas and I_a is the current of the sensor when exposed to air, which is called the baseline current. Analyte gases are injected into the sensing cell with controlled concentrations. Figure 3.5 shows a typical current-time plot showing the gas sensor response of the ZnO nanostructures to 16000 ppm H_2O vapour in air and 35000 ppm EtOH vapour in air. Before the sensing reaction, the sensor was pre-heated at 550 ℃ for over 2 hours in order to clean the surface. Then, the sensor is cooled to the sensing temperature and held at that temperature for 1 hour to obtain the baseline current I_a, which is marked as stage 1 in Figure 3.5. When the analyte gas is injected into the sensing chamber, the ZnO on the electrode interacts with the analyte gas, leading to a change in the resistance of through the material, as shown in stage 2; upon saturation with the analyte gas, the current curve trends to plateau, and I_g is recorded. Finally, the gas stream is switched to pure air and the recovery of the current to the baseline current is observed (stage 3). The sensing process was repeated five times to get precise data. For ethanol vapour, after the signal reaches the maximum value, i.e. stage 2 in Figure 3.5 (b), the current begins to drop, which is due to surface poisoning effects of carboxylate species formed on the surface.[5]

3.1.6 Response and recovery time

The response and recovery times are important parameters used for characterizing sensors. They are defined as the time required to reach 90% of the final, maximum change in current, when the analyte gas flow is turned on or off, respectively. The response/recovery time is applied to evaluate whether the sensor materials are rational candidates for commercial sensor materials.[6]

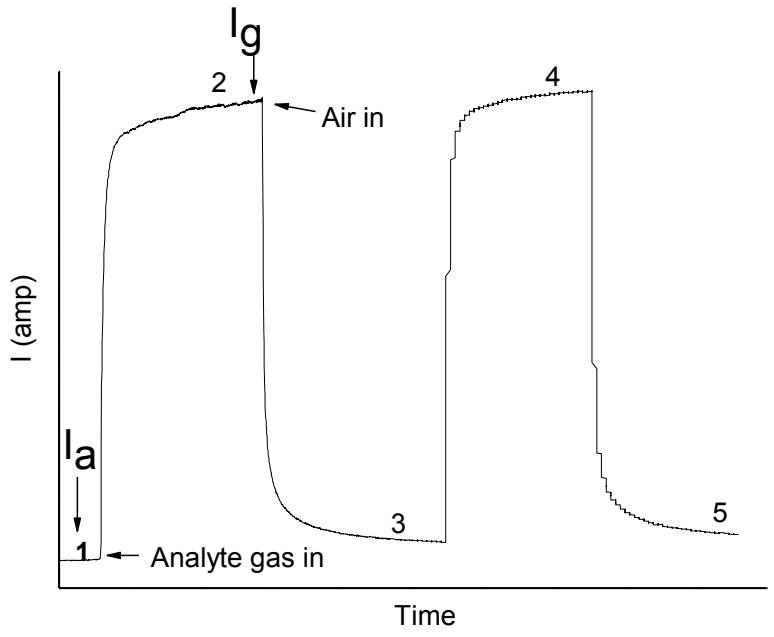

(a)

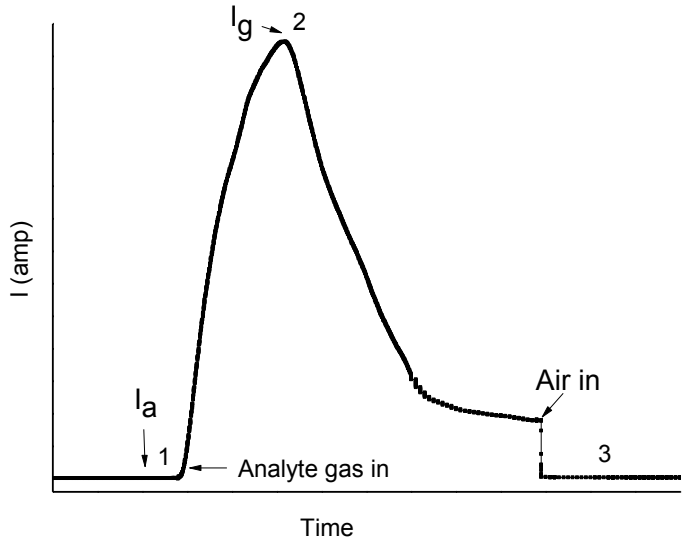

(b)

Figure 3.5 Typical current-time plots of gas sensor response to (a) 16000 ppm water vapour in air and (b) 35000 ppm ethanol vapour in air over ZnO nanowires.

3.2 Gas Sensing Performance of ZnO Nanowires Synthesized by Electrodeposition Method

3.2.1 Sensor responses of commercial zinc oxide powders

The sensitivity of the ZnO nanowires gas sensors greatly depends on the working temperature. At low temperatures (under 150 ℃), oxygen will trap electrons on the surface to produce O_2^- surface species, while O^- and O^{2-} are the predominant oxygen species at higher temperatures (150 – 450 ℃).[7] The effect of the temperature on device sensitivity was studied using ZnO gas sensors, and the sensing reactions were carried out with analyte gases at several sensing temperatures. The gas sensing properties of synthetic ZnO nanostructures were investigated with several analyte gases: saturated water vapour (16000 ppm) in air, saturated ethanol vapour (35000 ppm) in air, and 2000 (±5) ppm CO in air.

Commercial ZnO powders (ScholAR Chemistry, Lab Grade) with an average grain size of as 20 μm were used as the control to investigate the influence of temperature on sensing performance. 16000 ppm H_2O vapour in air was examined first, with measurements performed from 100 – 500 ℃, with 100 ℃ increments. Figure 3.6 shows the sensitivity-temperature plot of the commercial ZnO powder gas sensor for 16000 ppm H_2O vapour in air. It can be observed from the plot that the sensor shows the highest sensitivity at 100 ℃, and the sensitivity decreases as the working temperature increases. As water vapour is a common component of air, it is desirable to have low sensitivity to H_2O vapour for device applications, as high sensitivity to H_2O can give false signals towards other analytes in humid environments.

Investigation of 35000 ppm EtOH vapour in air was carried out at 300 and 500 ℃, and the sensitivities of the commercial ZnO powder are quite similar for EtOH at both temperatures: 18.8 at 300 ℃ and 19.8 at 500 ℃. The last analyte gas, 2000 ppm CO in air was tested with the commercial ZnO powder gas sensor at 300 ℃, and showed a low sensitivity of 2.63. The typical sensitivities of the commercial ZnO powder gas sensors to analyte gases are listed in Table 3.1.

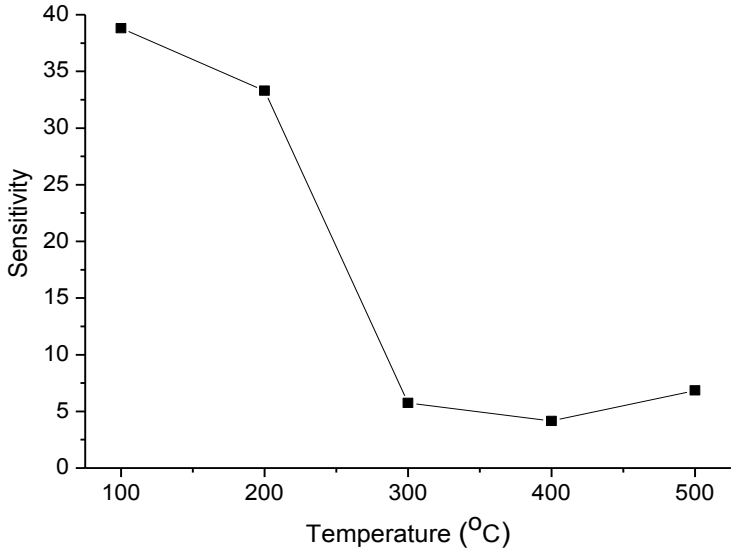

Figure 3.6 Sensitivity–temperature plot of commercial ZnO powder towards 16000 ppm water vapour in air.

Temp. (℃)	16000 ppm H_2O vapour in air	35000 ppm EtOH vapour in air	2000 ppm CO in air
100	38.8	-	-
300	5.53	18.8	2.63
500	6.85	19.8	1.0[ii]

-: Experiment was not carried out.

*: The sensor did not give measurable response; the sensitivity is treated as 1.0.

Table 3.1 Sensitivity of commercial ZnO powders towards analyte gases as a function of temperature.

3.2.2 Sensor responses of ZnO nanowires synthesized by electrodeposition route

Three synthetic ZnO nanowires samples with nanowires diameters of 31 ± 3 nm, 150 ± 12 nm, and 280 ± 30 nm, respectively, were prepared as described in section 2.1.2. For convenience, these three nanowires gas sensors will be referred to as 30 nm nanowires, 150 nm nanowires, and 300 nm nanowires, respectively.

The sensing performance of ZnO nanowires to 16000 ppm H_2O vapour in air were investigated at 100, 300 and 500 ℃. The sensitivities are listed in Table 3.2. The ZnO nanowires show the best sensitivity at 100 ℃, and sensitivity decreases as the sensing temperature increases, which is similar with the temperature-sensitivity trends of commercial ZnO powder gas sensors. The sensitivity of the ZnO nanowires towards H_2O vapour in air is quite high, around 1000, at 100 ℃, and at 300 ℃, the sensitivity is still above 100 for the 30 nm nanowires.

	16000 ppm H_2O vapour in air			**35000 ppm EtOH vapour in air**			**2000 ppm CO in air**		
Temp. (℃)	30 nm	150 nm	300 nm	30 nm	150 nm	300 nm	30 nm	150 nm	300 nm
100	1583	1213	923	-	-	-	-	-	-
300	141	79	53	368	291	204	1.63	1.53	1.41
500	2.86	2.68	1.98	20.2	15.8	10.4	1.0(*)	-	-

-: Experiment was not carried out.

*: the nanowires sensor did not give measurable response; the sensitivity is treated as 1.0.

Table 3.2 Sensing performance of ZnO nanowires synthesized by electrodeposition route.

The sensing performance of synthetic ZnO nanowires to 35000 ppm EtOH vapour in air was also studied. The sensitivity-temperature trends were first explored by sensing reactions carried out from 200 – 500 ℃, with 50 ℃ increments with 30 nm nanowires. From the results shown in Figure 3.7, the sensitivity of the ZnO nanowires to EtOH vapour reached a maximum near 300 ℃. The sensing performance of the other ZnO nanowires were investigated at 300 and 500 ℃, and the sensitivities are listed in Table 3.2 above. All the nanowires gas sensors have a high sensitivity to the EtOH vapour in air; at 300 ℃ all our nanowires sensors show sensitivities over 200, while the commercial ZnO powder had a sensitivity of approximately 19 under these conditions. All the ZnO nanowires synthesized by electrodeposition show much better sensitivity toward EtOH at 300 ℃ than that at 500 ℃.

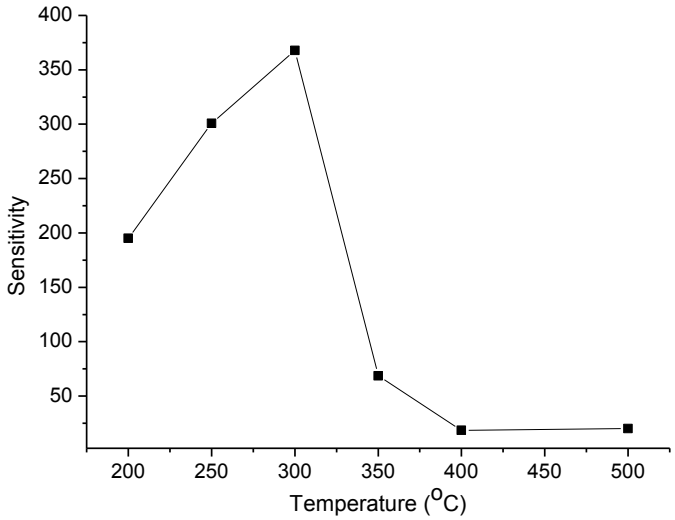

Figure 3.7 Sensitivity–temperature plot for 30 nm ZnO nanowires towards 35000 ppm ethanol vapour in air.

In the investigation of the sensing performance of the ZnO nanowires to 2000 ppm CO in air, the sensitivity – temperature plot was explored for the 30 nm nanowires from 250 – 500 ℃, with 50 ℃ increments. From Figure 3.8, one can see that the sensors show the best sensitivity at 300 ℃, which is close to the ideal sensing temperature for CO by ZnO materials seen by others in the literature.[8,9] The sensitivities of all the ZnO nanowires at 300 and 500 ℃ are listed in

Table 3.2 above. The sensitivity of the ZnO nanowires towards CO increases slightly as the diameter decreases, a size effect will be discussed in detail in section 3.3. It should be noted that the sensitivity of the nanowires towards CO is significantly lower than the commercial ZnO powders.

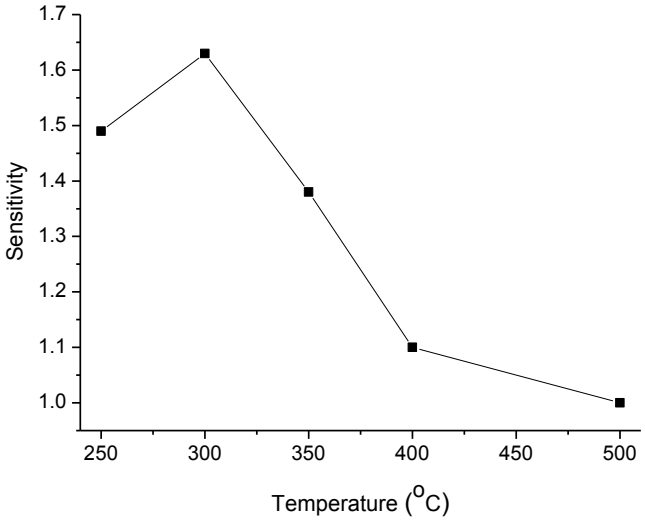

Figure 3.8 Sensitivity–temperature plot of 30 nm ZnO nanowires towards 2000 ppm CO in air.

3.2.3 Sensor responses of ZnO nanowires synthesized by the hydrothermal route

The gas sensor performance of ZnO nanorods synthesized by the hydrothermal route was examined for the same analyte gases above (section 3.2.2). The diameter of the ZnO nanorods is approximately 400 nm, and for convenience, the hydrothermal ZnO sample will be referred to as 400 nm nanorods in the following discussion. The sensing performance of the nanorods was investigated using the same experimental conditions as used for the ZnO nanowires.

Table 3.3 lists the sensitivities of ZnO 400 nm nanorods when exposed to 16000 ppm H_2O vapour in air, 35000 ppm EtOH vapour in air and 2000 ppm CO in air at 100, 300, and 500 ℃. Figure 3.9 (a) and b show the sensor response of the ZnO nanorods towards 16000 ppm H_2O vapour in air and 35000 ppm EtOH vapour in air, respectively. From Figure 3.9 (a), we note that the nanorods showed the highest sensitivity towards H_2O at 100 ℃, 2235, and the lowest

sensitivity towards H_2O was seen at 500 ℃. As seen in Figure 3.9 (b), the sensor response towards 35000 ppm EtOH in air is higher at 300 ℃ than that at 500 ℃; the sensitivity is 633 and 185 at these temperatures, respectively. The sensitivity vs. temperature trends of the nanorods is similar to those of the nanowires samples. In section 3.3, the sensor results for the nanorod samples to the electrodeposited nanowires sample will be compared in more detail.

Temp. (℃)	**16000 ppm H_2O vapour in air**	**35000 ppm EtOH vapour in air**	**2000 ppm CO in air**
100	2235	-	-
300	961	633	1.85
500	82	185	-

-: Experiment was not carried out.

Table 3.3 Sensitivity of 400 nm nanorods synthesized by the hydrothermal route to various gases.

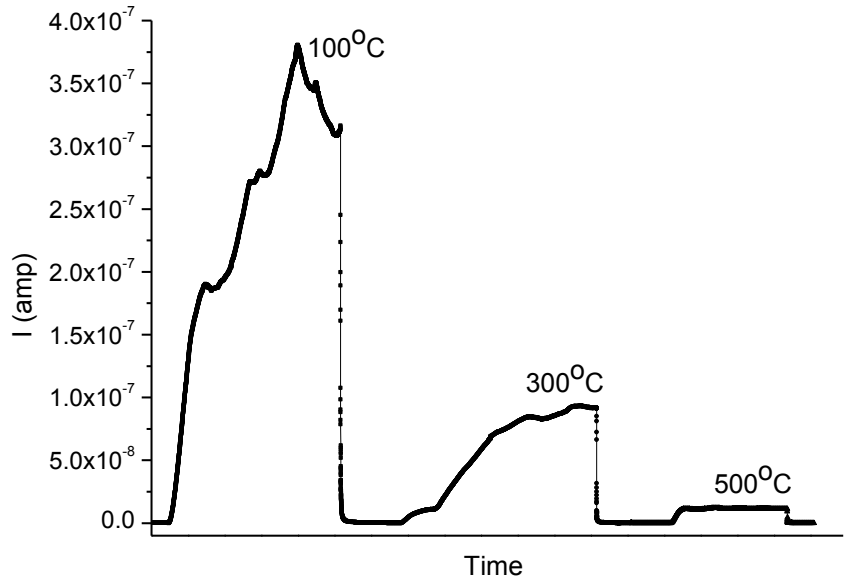

(a)

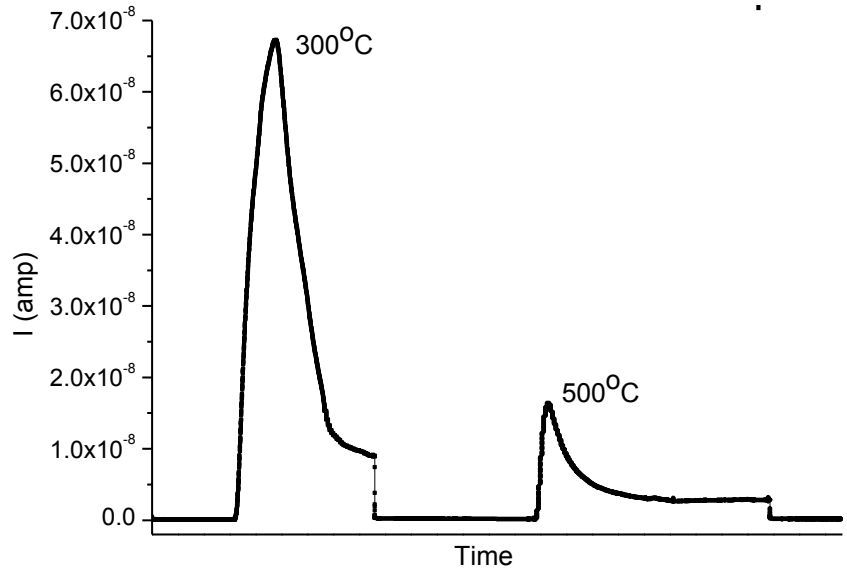

(b)

Figure 3.9 Sensitivity plots of 400 nm ZnO nanorods towards (a) 16000 ppm H_2O vapour in air and (b) 35000 ppm EtOH vapour in air.

3.3 Discussion and Comparison of Results

3.3.1 Investigation of ZnO nanowire sensors

3.3.1.1 Sensitivity: size dependence of sensing performance

As detailed in the discussion in chapter 1, the gas sensor properties of ZnO nanowires can be highly affected by the diameter of the nanowires. The sensitivity of ZnO nanowires synthesized by the electrodeposition route when exposed to 16000 ppm H_2O vapour in air at 100, 300, and 500 ℃ are shown in Figure 3.10 (a). Figure 3.10 (b) shows the sensitivity–temperature plot for the electrodeposited ZnO nanowires exposed to 35000 ppm EtOH in air at 300 ℃ and 500 ℃, and Figure 3.11 shows three plots for ZnO nanowires exposed to CO (2000 ppm) in air. As seen in Figure 3.10 and 3.11, in all cases, the ZnO nanowires synthesized by electrodeposition show increased sensitivity as the diameter decreases, which agrees with theory. As the diameter of the nanowires become smaller, and the dimension of the nanowires approaches the Debye length of ZnO (~ 30 nm),[9,10] all the ZnO atoms can be treated as surface atoms and the gas sensor shows the best sensor performance. The best responses are seen for the 30 nm nanowires, which show a sensitivity of 1583 for 16000 ppm H_2O vapour in air at 100 ℃, while the 300 nm nanowires have a sensitivity of 923 at the same temperature. In contrast, the commercial ZnO powder, which has an average grain size of 20 μm, has a sensitivity towards 16000 ppm H_2O vapour of 38.8 at this temperature. The same trend is observed for 35000 ppm EtOH vapour in air, the 30 nm nanowires show a sensitivity of 368 at 300 ℃, while at the same temperature, the 300 nm nanowires have a sensitivity of 204, and the commercial ZnO powder has a sensitivity of 18.8.

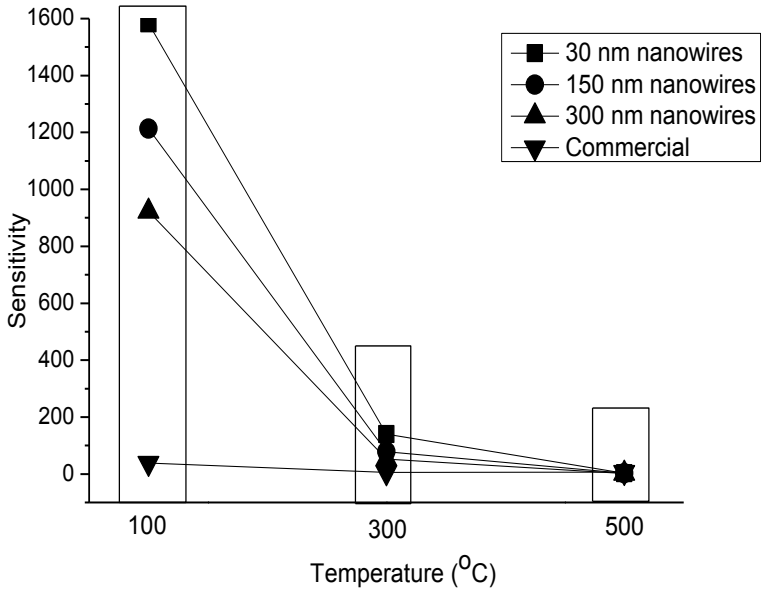

(a)

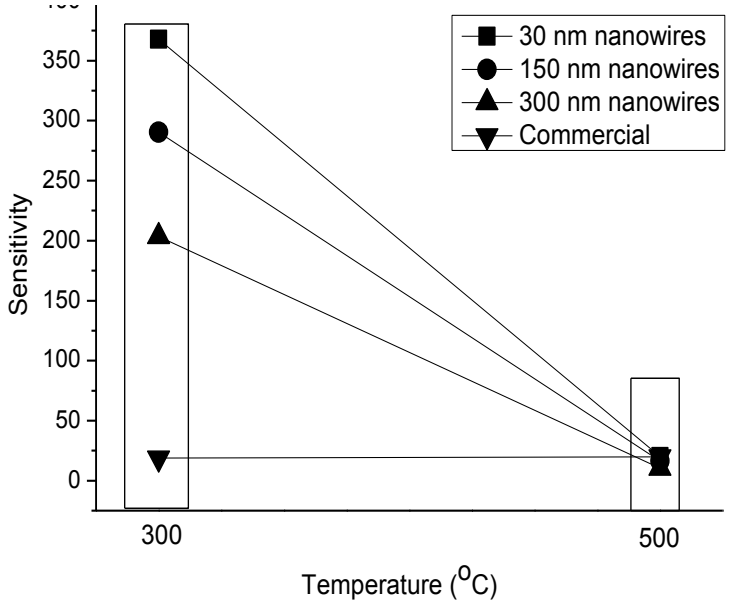

(b)

Figure 3.10 Sensitivity changes of electrodeposited ZnO nanowires to (a) 16000 ppm H_2O vapour in air, (b) 35000 ppm EtOH vapour in air.

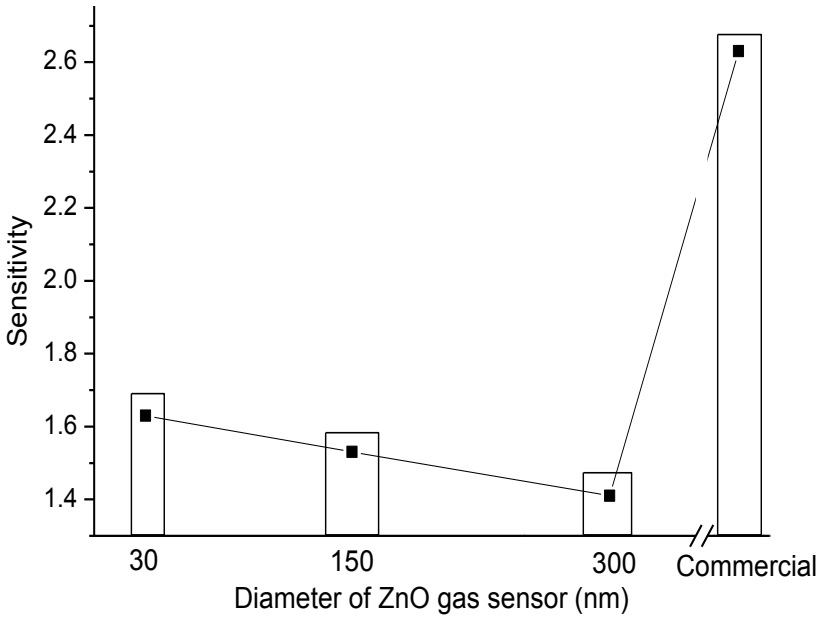

Figure 3.11 Sensitivity changes of electrodeposited ZnO nanowires to 2000 ppm CO in air.

3.3.1.2 Selectivity

Selectivity is another important property of gas sensors; selectivity is defined as the ability to recognize one analyte gas from others. We define the selectivity towards a specific gas is defined as selectivity = sensitivity (gas A)/Sensitivity (gas B). In order to investigate the selectivity of the ZnO nanowires towards specific gases, the sensitivities of these gas sensors when exposed to different analyte gases were compared at different sensing temperatures. The selectivity of the ZnO nanowires and the commercial ZnO powder at 300 and 500 ℃ are shown in Figure 3.12 (a) and (b), respectively. From these figures, it can be observed that at both 300 and 500 ℃, the ZnO nanowires show higher sensitivity to 000 ppm EtOH vapour in air than that to 16000 ppm H_2O vapour in air and 2000 ppm CO in air. For the 30 nm nanowires, at 300 ℃, the sensitivity towards EtOH is 368, which is higher than that the sensitivities towards H_2O (141) and CO (1.63), respectively, while at the 500 ℃, the sensitivity towards EtOH, H_2O and CO are 20.2, 2.86 and 1.00, respectively. The same trends could also be observed for other nanowires samples; all the nanowires sensors are highly selective towards EtOH as opposed to H_2O and CO.

Selectivity is also affected by the temperature; while the ZnO nanowires show higher responses towards 35000 ppm EtOH vapour in air than to 16000 ppm H_2O vapour in air at both 300 and 500 ℃, the data shows that the selectivity towards EtOH at each temperature is different. The selectivity of the nanowires sensors and commercial ZnO powder towards 35000 ppm EtOH vapour in air vs. 16000 ppm H_2O vapour in air are listed in Table 3.4. At 300 ℃, the selectivity of 30 nm nanowires towards EtOH vs. H_2O is 2.62, while it is 7.06 at 500 ℃, which means at higher temperatures, the ZnO nanowires gas sensors can discriminate better between saturated EtOH vapour and water. This is very important as most sensor applications take place in ambient air conditions, which can have highly variable humidity. The same selectivity trend could also be observed for other nanowires sensors. For the 300 nm nanowires, at 500 ℃, the selectivity between two analyte gases is 5.25, which is higher than that at 300 ℃ (3.88).

Size (nm)	**Selectivity**		
	EtOH vs. H_2O		**EtOH vs. CO**
	300 ℃	500 ℃	300 ℃
30	2.62	7.06	226
150	3.69	6.08	190
300	3.88	5.25	145
Commercial	3.40	3.58	7.12

Table 3.4 Selectivity of 35000 ppm EtOH vapour in air vs. 16000 ppm H_2O vapour in air and 2000 ppm CO in air.

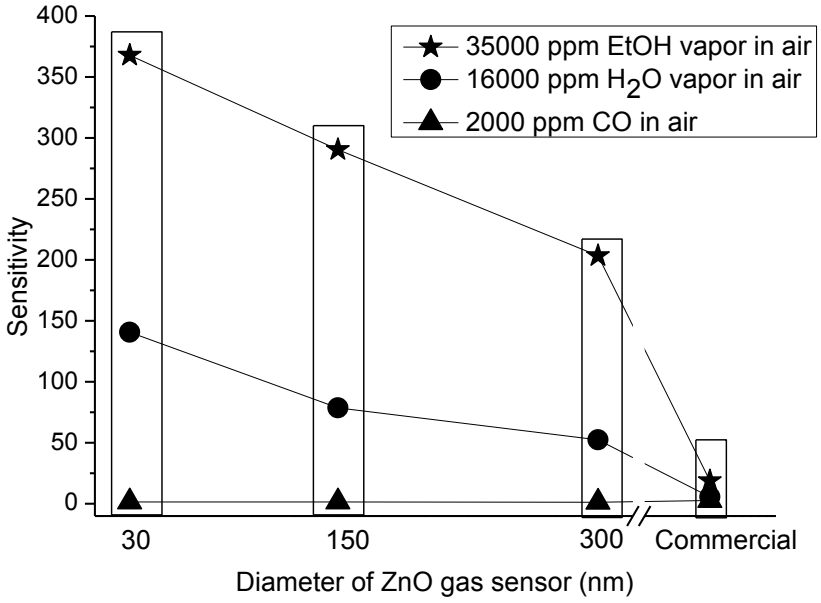

(a)

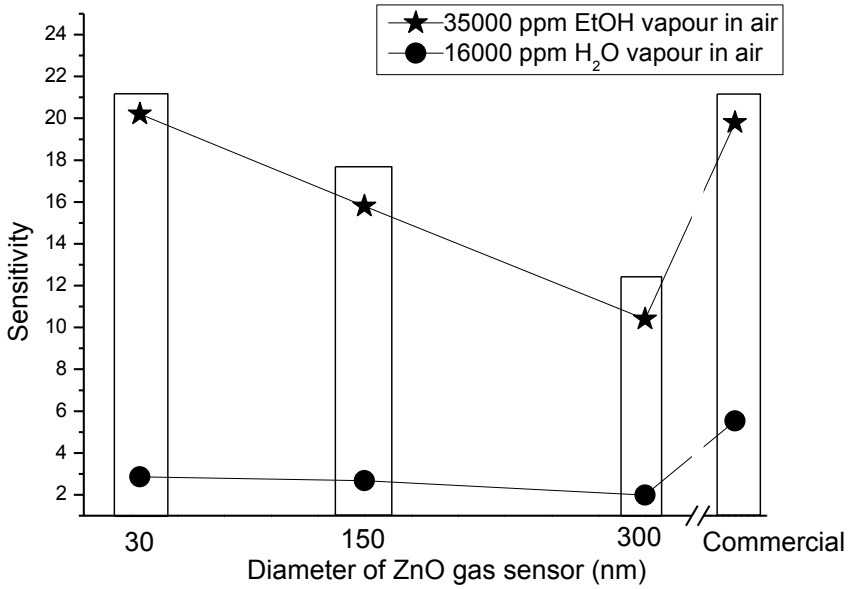

(b)

Figure 3.12 Sensitivity-diameter plots of the ZnO nanowire gas sensors at (a) 300 ℃ and (b) 500 ℃.

It should be noted that the size dependence is also affecting the selectivity; as the 30 nm nanowires shows better selectivity towards EtOH than H_2O and CO than the 150 nm and 300 nm nanowires. For the commercial ZnO powder, although the sensors are still selective towards EtOH as opposed to H_2O and CO, the sensitivity does not differ much upon changing the sensing temperature; the selectivity of EtOH vs. H_2O is 3.40 at 300 ℃, and 3.58 at 500 ℃. The selectivity of the nanowires sensors to EtOH vs, CO is much higher than that of the H_2O vapour, as the sensitivity of the nanowires sensors to CO is quite low. At 300 ℃, the selectivity of EtOH vs. CO is 226 for the 30 nm nanowires, 190 for the 150 nm nanowires and 145 for the 300 nm nanowires. It should be noted that the commercial ZnO powder does not have the same ability to distinguish the EtOH from CO, at 300 ℃ the selectivity is only 7.12, which is much lower than the nanowire sensors.

3.3.1.3 Response and recovery time

Response/recovery time is another factor used to evaluate the performance of gas sensors; both are defined herein as the time taken to achieve 90% of the final change in resistance following the change of gas concentration. Table 3.5 shows the response and recovery time of ZnO nanowires to 16000 ppm H_2O vapour in air at three sensing temperatures. From the table, one can see that the response time of the gas sensors decreases dramatically as the temperature increases, as expected from the Arrhenius equation as shown in eq 3.2.

$$k = A\exp(\frac{E_a}{RT}) \tag{3.2}$$

At low temperatures, the sensors need 10 - 15 minutes to response to the 16000 ppm H_2O vapour in air; while at high temperatures, it only takes several seconds for the sensor to show a maximum response to the analyte gas. However, the recovery time does not change appreciably with the temperature, and all the sensors showed good abilities to recover from exposure to the analyte gas.

For 35000 ppm EtOH vapour in air, the response time and recovery times show similar tendencies to those for 16000 ppm H_2O vapour in air, as shown in Table 3.6. Again the response time decreases as the sensing temperature increases, while the recovery time remains at similar

levels throughout. The sensitivity of ZnO nanowires sensors to CO are very low (not shown), and both the response and recovery time are quite short; between 1 to 5 seconds at all temperatures studied. The results show that a higher temperature is desirable for fast, effective responses towards EtOH and H_2O vapours. In contrast the response and recovery time of the commercial ZnO powders is much different from the nanowires. At low temperatures, the response and recovery time of commercial powders are smaller than the nanowires sensors; however, at higher temperature, the nanowires gas sensors have much faster response times than commercial ZnO powders. This bodes well for the use of ZnO nanowires as improved gas sensors. From the data of response and recovery time, we find that less time is needed as sensing temperature increase. In addition, nanowires with smaller diameters should have larger surface areas, which should leads to shorter response and recovery time. However, while there is a slight trend towards faster responses with smaller diameters, it is imperfect.

Size (nm)	**Response time (sec)**			**Recovery time (sec)**		
	100 ℃	**300 ℃**	**500 ℃**	**100 ℃**	**300 ℃**	**500 ℃**
30	1600	314	3	12	16	6
150	2132	441	4	11	35	16
300	1203	307	4	10	87	10
Commercial	722	1510	925	4	32	32

Table 3.5 Response and recovery time of ZnO nanowire sensors towards 16000 ppm H_2O vapour in air.

Size (nm)	Response time (sec)		Recovery time (sec)	
	300 ℃	**500 ℃**	**300 ℃**	**500 ℃**
30	55	34	3	7
150	107	14	4	5
300	188	23	3	23
Commercial	121	67	1	87

Table 3.6 Response and recovery time of ZnO nanowire sensors towards 35000 ppm EtOH vapour in air.

3.3.2 Investigation of ZnO nanorod gas sensors

3.3.2.1 Sensitivity: shape dependence of sensing performance

The other nanostructured ZnO material studied for its sensor performance was the ZnO nanorods synthesized by a hydrothermal route, which will be referred to as 400 nm nanorods. The sensing performance of the 400 nm nanorods was compared with the ZnO nanowires synthesized by the electrodeposition route. Figure 3.12 shows sensitivity-temperature plots at 300 and 500 ℃, respectively, for both sensors towards 16000 ppm H_2O and EtOH vapour in air. According to the diameter vs. Debye length discussion in chapter 1, the 400 nm nanorods should have the lowest sensitivity of the nanostructured samples given their larger diameters, but should still have significantly better sensing performances than the commercial ZnO powders. However, examination of the data leads to a different conclusion. From Figure 3.13, it can be noted that the 400 nm nanorods show quite high sensitivities towards 16000 ppm H_2O vapour in air and 35000 ppm EtOH vapour in air at both 300 and 500 ℃. The data shows that the sensing performance of the 400 nm nanorods towards the analyte gases is not only greater than that of 300 nm nanowires, but even greater than the 30 nm nanowires as well. For 16000 ppm H_2O vapour in air at 100 ℃, the 400 nm nanorods show a very high sensitivity of 2235, while the 30 nm nanowires have a

sensitivity of 1583. The same trend can be observed at 300 ℃, the 400 nm nanorods have a sensitivity towards H_2O of 961, while the 30 nm nanowires have a sensitivity of 141. Similarly, for responses towards 35000 ppm EtOH vapour in air at 300 ℃, the 400 nm nanorods have a sensitivity of 633, which is also higher than that of the 30 nm nanowires (291).

The SEM images of the 400 nm ZnO nanorods synthesized by the hydrothermal route (Figure 2.10) and 300 nm ZnO nanowires synthesized by electrodeposition (Figure 2.5) show that along with the difference in diameters between these samples, the shapes are also different. For the samples synthesized by electrodeposition route, the aspect ratio (length:width) of individual nanowires is over 200:1, while the aspect ratio of the nanorods is only approximately 4:1. Thus the nanorods have much shorter lengths than those of the nanowires studied, and thus, the nanorods have a higher total surface area than nanowires with smaller widths, the 400 nm nanorods have 42% more surface area which could participate in the sensing reaction than that of the 300 nm nanowires. The nanorods have a small aspect ratio, thus the sensing response of the nanorods are much more dependent on grain boundary effects between nanorods than the effect of the diameter of the individual rods, the result of which is that the nanorods show a higher sensitivity towards analyte gases than the nanowire sensors with much smaller diameters.[11]

3.3.2.2 Selectivity

For the 400 nm nanorods, the selectivity also changes with temperature. Figure 3.14 shows the sensitivity-size plot of our ZnO gas sensors. At 500 ℃, as shown in Figure 3.14 (b), the 400 nm nanorods show the highest responses towards both 35000 ppm EtOH vapour in air and 16000 ppm H_2O vapour in air; thus the selectivity towards ethanol is only 1.35, which is only approximately 25% of the value of the selectivity towards ethanol for the nanowires. At 300 ℃, the selectivity of 400 nm nanorods towards EtOH vs. H_2O is 0.66, which means they respond better to H_2O vapour than the EtOH vapour. This is completely different than the response of the nanowire sensors, which always showed higher responses to ethanol. In this case, although the nanorods have a good sensitivity towards EtOH vapour, it is not a good candidate as an EtOH sensor because at moderate temperatures, the sensor has a high sensitivity to H_2O vapour as well. Thus the nanorods do not have the ability to distinguish EtOH from H_2O. However, it should be

noted that at 300 ℃, the nanorods sensors do show a good selectivity of EtOH vs. CO, 342, which is almost twice that of the nanowire sensors. The selectivity of 400 nm nanorods are listed below in Table 3.7 with two nanowires sensors added to contrast the results.

Sample	**Selectivity**		
	EtOH vs. H_2O		**EtOH vs. CO**
	300 ℃	**500 ℃**	**300 ℃**
30 nm nanowires	2.62	7.06	226
300 nm nanowires	3.88	5.25	145
400 nm nanorods	0.66	1.35	342

Table 3.7 Selectivity of nanorods and nanowires towards 35000 ppm EtOH vapour in air vs. 16000 ppm H_2O vapour in air and 2000 ppm CO in air.

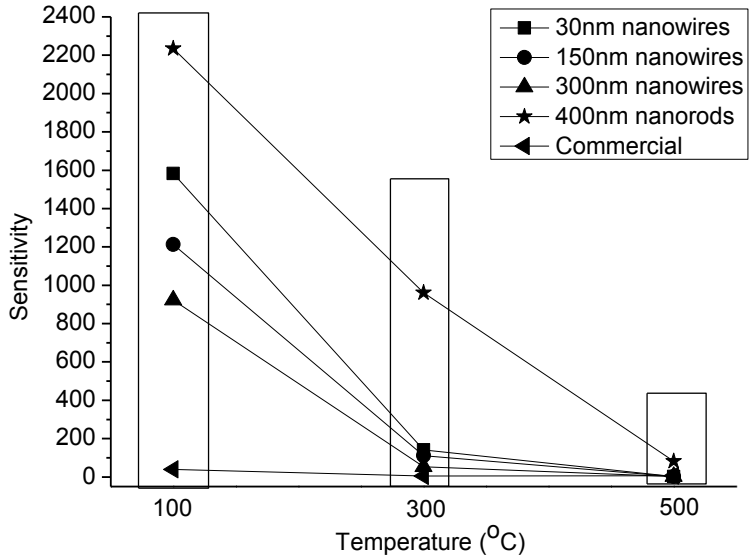

(a)

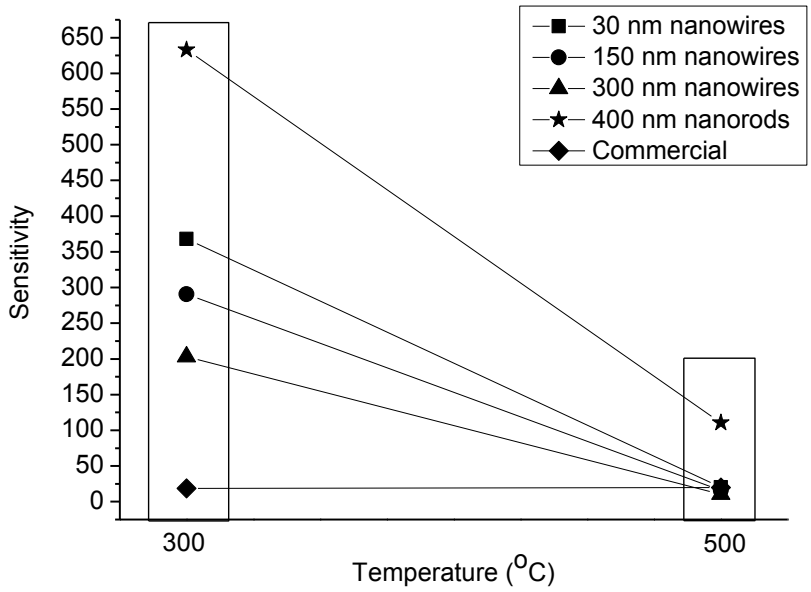

(b)

Figure 3.13 Sensitivity-temperature plots of the ZnO gas sensors at 300 ℃ and 500 ℃ towards (a) 16000 ppm H_2O vapour in air and (b) 35000 ppm EtOH vapour in air.

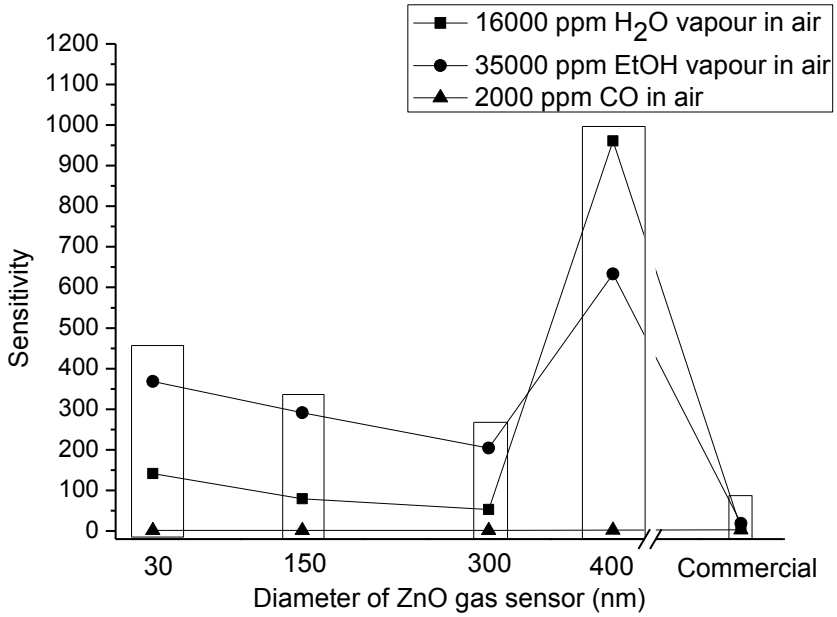

(a)

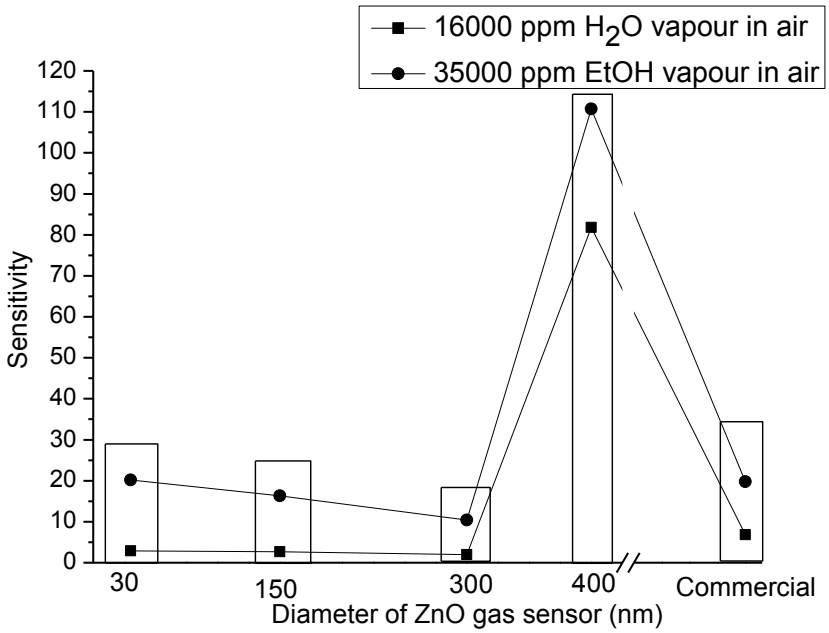

(b)

Figure 3.14 Sensitivity-size plot of ZnO gas sensors at (a) 300 ℃ and (b) 500 ℃.

3.3.2.3 Response and recovery time

The response and recovery time of the 400 nm nanorods were studied for the gas sensing reactions and are shown in Table 3.8, with 300 nm nanowires data listed to contrast the results. The response time of the sensors towards 16000 ppm H_2O vapour in air is much longer than that of the nanowires (between 10 min to 1 h), while the nanowires need only several minutes at lower temperatures, and only several seconds at 500 ℃. The response time of 400 nm nanorods towards 35000 ppm EtOH vapour in air is similar to that of the nanowire sensors. The 400 nm nanorods have good recovery ability; it took only several seconds for the sensors to recovery to the baseline at the sensing temperatures for all the analyte gases. Nevertheless, the high response times for these nanorod sensors, along with their poorer ability to discriminate between EtOH and H_2O vapours, suggest that the nanowires are better candidates for gas sensor design.

Sample	**16000 ppm H_2O vapour in air**					
	Response time (s)			**Recovery time (s)**		
	100 ℃	**300 ℃**	**500 ℃**	**100 ℃**	**300 ℃**	**500 ℃**
300 nm nanowires	1203	307	4	10	87	10
400 nm nanorods	3000	3100	345	4	34	1
	35000 ppm EtOH vapour in air					
	Response time (s)			**Recovery time (s)**		
	300 ℃		**500 ℃**	**300 ℃**		**500 ℃**
300 nm nanowires	188		23	3		23
400 nm nanorods	170		55	1		10

Table 3.8 Response and recovery times of 300 nm ZnO nanowires and 400 nm ZnO nanorods to different analyte gases.

3.4 Comparison of Nanoscale Sensors to Literature

The sensitivity of both the synthetic ZnO nanostructures produced in this work and ZnO nanostructures in the literature for sensing ethanol and CO vapours with different concentrations in air are listed in Tables 3.9 and 3.10, respectively. From the data in the Table 3.9, it is apparent that the synthetic ZnO nanostructures are over 10 times more responsive towards ethanol than the results listed in the literature at 300 ℃; even though much higher concentrations are used in this study, these values are still impressive. Cui and coworkers examined ZnO nanoparticles with diameter of 10 – 20 nm and found that they had a sensitivity of 20 towards 3000 ppm ethanol,[6] while Xu and his group investigated 60 nm ZnO nanorods and found that they had a sensitivity of 50 towards 2000 ppm ethanol.[12] However, at 500 ℃, our 400 nm nanorods shows similar sensitivity towards ethanol and are much more responsive than the ZnO nanowires.

ZnO nanostructures do not show very good sensitivity to carbon monoxide as one can see from Table 3.10. The sensitivity of nanostructured ZnO semiconductor gas sensors to detect CO is quite low, especially compared with the results for ethanol above. At an elevated temperature around 300 ℃, all the ZnO nanostructures had sensitivities towards 2000 ppm CO of between 1 and 2. Sun and coworkers worked on the 30 nm nanorods and found a sensitivity of 2 towards 200 ppm CO. In another case, the commercial ZnO powders with an average diameter of 20 μm showed the best response of 2.65, which is about two times the response of the nanoscale ZnO sensors studied here.

There are few papers discussing ZnO nanostructures as water vapour sensors, however, from our study, the ZnO nanostructures show a good sensing response to water vapour at relatively low temperatures, while this sensitivity decreases with increasing temperature. Water vapour is one of the most important gases in gas sensing work, as it is present in most working conditions. In order to detect ethanol vapour, the selectivity of ethanol vapour to water vapour is quite important. From our data, at elevated temperatures, our synthetic ZnO nanostructures could be as high as seven times more responsive to ethanol vapour as to water vapour. Unfortunately, we were not able to find appropriate comparisons in the literature with regards to sensitivity to water.

The response time and recovery time of ZnO nanostructures as sensors to detect target gases are quite reasonable. Upon comparison of the literature data and data in this study, the response and recovery times commonly are only seconds to several minutes. Xu and his groups studied the

detection of 60 nm ZnO nanorods to 2000 ppm ethanol and found that the response and recovery times were 10 and 30 seconds, respectively,[13] which is close to the data shown above. Thus makes the ZnO nanostructures synthesized in this study a promising candidate for commercial sensors.

		Temp. (℃)	**300 ±50**	**500 ±50**	
		Sensing gas Conc. (ppm)	**Sensitivity**	**Sensitivity**	**Ref.**
Literature	15 nm nanoparticles	3000	20		[13]
	25 nm nanowires	200	47		[12]
	60 nm nanorods	2000	50		[14]
	95 nm nanorods	1000		100	[13]
This work (synthetic)	30 nm nanowires	35000	**367.9**	**20.2**	
	150 nm nanowires	35000	**290.5**	**15.8**	
	300 nm nanowires	35000	**203**	**10.4**	
	400 nm nanorods	35000	**633**	**110.7**	

Table 3.9 Comparison of sensor results for ZnO nanostructures for detecting ethanol vapour from the literature and this study.

			Temp. (℃)	300 ±50	
			Sensing gas Conc. (ppm)	**Sensitivity**	**Ref.**
Literature		37.5 nm nanorods	50	1	[15]
		30 nm Nanorods	200	2	[16]
This work	(synthetic)	30 nm nanowires	2000	**1.63**	
		150 nm nanowires	2000	**1.53**	
		300 nm nanowires	2000	**1.41**	
		400 nm nanorods	2000	**1.85**	
	(Commercial)	20 μm powders	2000	**2.65**	

Table 3.10 Comparison of sensor results for the ZnO nanostructures for detecting CO from literature and this study.

3.5 References

(1) Wöllenstein, J.; Plescher, G.; Kuhner, G.; Böttner, H.; Niemeyer, D.; Williams, D. E. *IEEE Sens. J.* **2002**, *2*, 403-408.

(2) Sato, H.; Yoshimine, K.; Otsuka, T.; Shoji, S. *J. Micromech. Microeng.* **2007**, *17*, 909-914.

(3) Font, J.; Muntasell, J.; Cesari, E. *Mater. Res. Bull.* **1999**, *34*, 2221-2230.

(4) Foss, C. A.; Hornyak, J. G. L.; Stockert, J. A.; Martin, C. R. *J. Phys. Chem.* **1994**, *98*, 2963-2971.

(5) Chatterjee, A. P.; Mitra, P.; Mukhopadhyay, A. K. *J. Mater. Sci.* **1999**, *34*, 4225-4231.

(6) Simon, I.; Bârsan, N.; Bauer, M.; Weimar, U. *Sens. Actuators B* **2001**, *73*, 1-26.

(7) Mishra, V. N.; Agarwal, R. P. *Microelectron. J.* **1998**, *29*, 861-874.

(8) Kohl, D. *Sens. Actuators* **1989**, *18*, 71-113.

(9) Kolmakov, A.; Zhang, Y.; Cheng, G.; Moskovits, M. *Adv. Mater.* **2003**, *15*, 997-1000.

(10) Harrison, P. G.; Willett, M. J. *Nature* **1988**, *332*, 227-339.

(11) Jose, J.; Khadar, M. A. *Mater. Sci. Eng., A* **2001**, *304-306*, 810-813.

(12) Xu, H.; Liu, X.; Cui, D.; Li, M.; Jiang, M. *Sens. Actuators, B* **2006**, *114*, 301-307.

(13) Xu, J.; Chen, Y.; Chen, D.; Shen, J. *Sens. Actuators, B* **2006**, *113*, 526-531.

(14) Wan, Q.; Li, Q. H.; Chen, Y. J.; Wang, T. H.; He, X. L.; Li, J. P.; Lin, C. L. *Appl. Phys. Lett.* **2004**, *84*, 3654-3656.

(15) Lv, Y.; Guo, L.; Xua, H.; Chu, X. *Physica E* **2007**, *36*, 102-105.

(16) Cho, P. S.; Kim, K. W.; Lee, J. H. *J. Electroceram.* **2006**, *17*, 975-978.

CHAPTER 4
CONCLUSIONS AND FUTURE WORK

4.1 Summary of ZnO Nanostructures and Their Sensing Property

By the methods of electrodeposition and hydrothermal synthesis, four different ZnO nanostructures were synthesized, and the sensing properties of these ZnO nanostructures were studied by investigation their electrical response towards water, ethanol, and carbon monoxide vapours. The nanostructures synthesized by electrodeposition route were nanowires synthesized in different AAO templates with final nanowires diameters of 31 $\pm$3 nm, 150 $\pm$12 nm, and 280 $\pm$30 nm, respectively, while the length is 10 $\pm$2 μm for all samples. Nanorods were prepared by a hydrothermal method from ZnO nanoparticle seeds and have an average diameter of 350 $\pm$20 nm, and length of 2.5 μm.

With regards to sensing performance, the synthetic ZnO nanowires and nanorods show high sensitivity towards both saturated water vapour (16000 ppm) in air and saturated ethanol vapour (35000 ppm) in air and minimal sensitivity towards CO. For commercial applications, it is desirable to have a sensor which has high sensitivity to alcohol and low sensitivity to water, along with fast response and recovery times. Low sensitivity towards water is important as the H_2O is commonly present in the air and the sensor should not give false readings for humidity. From the sensitivity, selectivity, response and recovery time data, the nanowires synthesized by electrodeposition with a diameter of 31 $\pm$3 nm are the best candidate for commercial gas sensors. These nanowires have good selectivity towards saturated ethanol vapour in air compared to saturated H_2O vapour in air. At high temperature (500 ℃), the nanowires are seven times more responsive to ethanol than water, and at moderate temperatures (300 ℃), this value is 2.6. Meanwhile, the selectivity of these nanowires for EtOH against 2000 ppm CO in air is quite high, our nanowires is over 200 times more responsive to ethanol than CO. The 30 nm nanowires have good sensor response and recovery, as the sensing reaction to EtOH is complete within 1 minute, while only several seconds are needed for full recovery. However, at room temperature, while the sensors show good responses to ethanol, they did not show good selectivity saturated EtOH vapour in air against saturated H_2O vapour in air; thus such ZnO nanostructures must be used at elevated temperatures for commercial applications.

4.2 Future Work

4.2.1 Continuing directions

Further research could focus on the ZnO nanorods synthesized by hydrothermal route with smaller diameters. It would be interesting to see how the sensitivity and selectivity of these sensors changed as size of these nanorods approach to the Debye length; results with the 400 nm nanorods suggest shorter nanorods with smaller diameters should have greater sensitivities.

A second direction would be to inspect the sensing behaviour of the ZnO nanostructures, include nanowires and nanorods, to the target gases with lower concentrations, and determine both the detection limits of these sensors and the concentration dependence of the sensor response.

Finally, in the sensing experiments in Chapter 3, we found out that at 500 ℃, the commercial ZnO powder with an average grain diameter of 20 μm showed mild responses to EtOH vapour and water vapour, but showed much higher sensitivity towards CO than the nanoscale sensors examined. This phenomenon could not be explained by the size effect mechanism and should be investigated in the future. In addition, the commercial powders showed higher responses to EtOH and water at 300 ℃ than at 500 ℃; this behaviour was not seen for the nanoscale systems.

4.2.2 Nanobarcodes

Metal-doped ZnO nanostructures are an attractive subject which might be good candidates as nanoscale gas sensors at both room temperature and elevated temperatures. Nanobarcodes are cylindrically-shaped nanowires, in which compositions can be alternated along the length. Natan and coworkers described in 2001 the synthesis of nanobarcodes consisting of multi-layered gold, silver, nickel and other metal in segments as short as 10 nm and as long as several micrometers, such as Au/Ag/Au and Au/Ag/Ni/Pd/Pt nanobarcodes by a template route with electrodeposition. Nanobarcodes have been widely in biology and non-biology, ranging from product tracking to multiplexed biodetection. [1-3]

Multi-metallic nanowires were synthesized to investigate their gas sensing properties. For example, in a three-layered nanobarcode composed by gold/zinc oxide/gold (refered to as Au/ZnO/Au), the length of the ZnO segments could be controlled during the synthesis process, ranging from several nm to hundreds of nanometers. A schematic model for the grain-size effect is shown in Figure 4.1. For single-crystalline ZnO nanowires, the grain size D (or length of the nanowires) would be considerably greater than the Debye length L, and the electrical conduction would then be controlled by the grain boundaries. However, for short ZnO segments in nanobarcodes, reducing the grain size D below 2L would cause the grain resistance to dominate the resistance of the whole nanowire, with should dramatically increase sensitivity. The grain control model is the most sensitive condition, thus the ZnO nanobarcodes with smaller grains sizes should be more sensitive than the ZnO nanowires with larger size.[4-6]

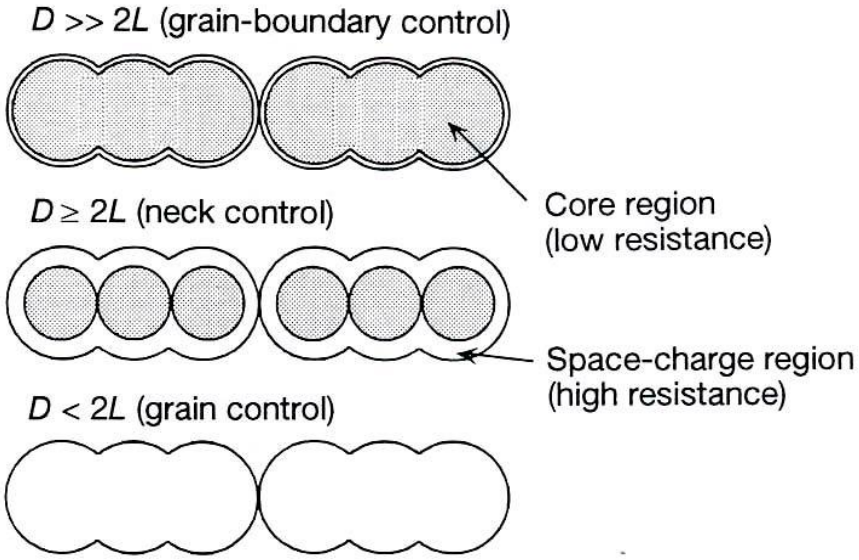

Figure 4.1 Schematic models for grain-size effects.[6] (Adapted with permission from reference 6. Copyright 1999 MRS.)

The Au/ZnO/Au multimetallic nanowires are composed by alternating layers of Au and ZnO. The nanobarcodes were synthesized by an electrodeposition route, similar to the synthesis of the Zn/ZnO nanowires described in chapter 2. The barcode nanowires were grown within the pores of an AAO template from the cathode of the custom-made deposition cell, as

shown in Figure 2.2, and the composition of the wires is varied by changing the species to be electrodeposited. The individual length of barcode segments can be controlled by varying the total charge in each deposition step. Briefly, the synthesis of Au/ZnO/Au nanobarcodes consists of a multiple step procedure. Before electrodeposition, a layer of silver gel (colloidal silver in acetone base, EMS) is painted onto the backside of the AAO membrane, and serves as the conducting cathode lead while a piece of bulk metal wire served as the anode. The Au aqueous electrolyte solution utilized as an Au plating solution was purchased commercially (Technic Inc.) and 2% by weight gelatin was added under vigorous stirring. Then, the AAO template was impregnated by the Au electrolyte solution and ultrasonicated to remove any trapped gas inside the pores. Electrodeposition was carried out in a custom-made plastic cell as shown in Figure 2.2 with the template backside (silver layer) facing downwards and connected to the cathode of the DC power-supply (Solartron SI1287/SI1260). First, a layer of Au nanowires were electrodeposited as the first layer of the nanobarcodes within the pores of the AAO template with pore diameters of 100 nm. The electrodeposition was carried out under galvanostatic conditions with a 1 mA current for 20 minutes. Au ions are reduced at the cathode and deposited on the silver layer while gold was oxidized at the anode during the electrodeposition to replenish the Au^{3+} cations. After the deposition of the first Au layer, the Au electrolyte solution was then removed and the deposition cell was thoroughly cleaned by deionized water. Then the Zn layer was electrodeposited onto the Au layer by the same synthetic process as previously described in the synthesis of pure Zn nanowires in chapter 2 for 2 hours. This was followed by removal of the Zn electroplating solution and thorough washing of the deposition cell. Finally, the second Au layer was deposited on the top of the previous Zn layer following the methodology of the first Au electrodeposition. The length of each of the components of the nanowires could be controlled by adjusting the time of deposition, as the total amount of the charge for each of the segment were carefully calculated by Faraday's Law (eq 2.3). The last step of the synthesis was to anneal the multisegment nanowire in a furnace at 550 ℃ for 5 hours under O_2.[7,8] This step was taken to oxidize the Zn segment to ZnO. The nanowires were then released from the pores of the template by dissolving the Al_2O_3 template in 2.0 M NaOH solution. The Au layers on the top and bottom of the nanowires protected the central ZnO segments from dissolution in the presence of the strong base.

The resulting Au/ZnO/Au nanowires were characterized by optical microscopy to observe their structures. The nanowires were dispersed by ultrasonication in deionized water for 5 minutes, and then spread on a glass substrate. The nanowires were observed to be quite pure of bulk impurities from optical microscopy images, as shown in Figure 4.2. The average single nanowire has a length of 5.6 ± 1.5 μm and a diameter of 136 ± 15 nm, which is close to dimensions of the Zn nanowires synthesized from 100 nm AAO templates. Figure 4.2 (b) is an optical microscopy image of a single wire; the bright part of the wire is Au and the dark part is likely ZnO. Unfortunately, optical microscopy could not conclusively indicate whether the desired Au/ZnO/Au nanowires were formed; Figure 4.2 (b) suggests possible decomposition into Au/ZnO or Au and ZnO segments during the calcination or the isolation processes.

The presence of both crystalline Au and ZnO components of the nanowires could be confirmed from the pXRD pattern, which is shown in Figure 4.3. Energy dispersive X-ray (EDX) spectroscopy was also carried out to determine the bulk elemental compositions of the nanowires. From the EDX profile in Figure 4.4, the nanowires were composed of Au and Zn; the C and Si signals are from the carbon tape. However neither of these techniques was able to definitely prove that the ZnO/Au/ZnO structure remained intact; future work on single-nanowire EDX would likely allow for determination of the structural integrity of the nanowires.

Further investigation is required for the deeper understanding of the potential for multi-segment nanowires for gas sensor research. We might expect to see better sensitivity for the ZnO nanobarcodes compared to pure ZnO nanostructures. Electrodeposition could be employed as an effective route to synthesize other nanobarcodes. Nanobarcodes with multiple-layers of Au and ZnO segments, as well as nanobarcodes composed of other metals and semiconductors could be synthesized. In addition, in the electrodeposition route, nanobarcodes could be prepared with variety of dimensions by using different growing templates with different lengths and diameters, while the sizes of each segment also could be managed by adjusting the time of deposition. Electron microscopy such as SEM, TEM can be employed for the determination of the formation of the nanobarcodes, while x-ray diffraction and/or electron diffraction can be applied to test the crystallinity of each segment.

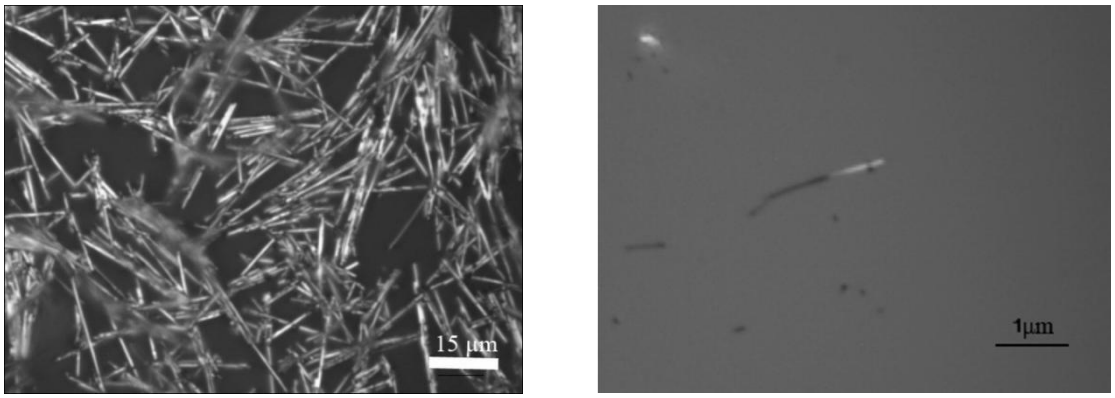

(a) (b)

Figure 4.2 Optical microscopy images for Au/ZnO/Au nanobarcodes.

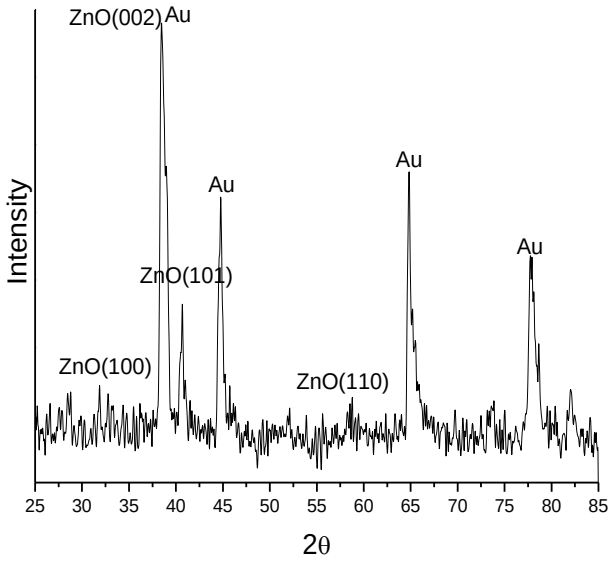

Figure 4.3 Powder XRD pattern of Au/ZnO/Au nanobarcodes.

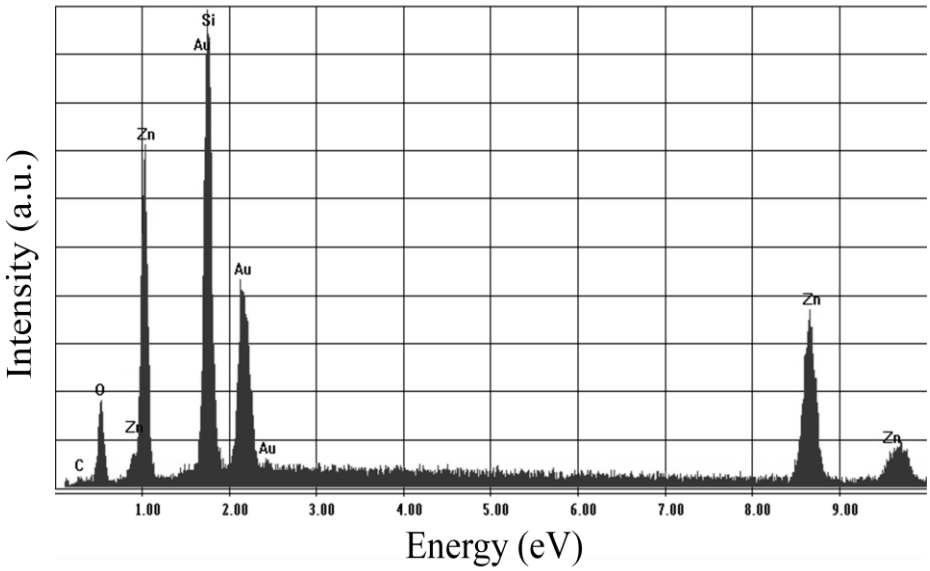

Figure 4.4 EDX spectrum of Au/ZnO/Au nanobarcodes.

4.3 References

(1) Wang, J. *J. Mater. Chem.* **2008**, *18*, 4017-4020.

(2) Nicewarner-Pena, S. R.; Freeman, R. G.; Reiss, B. D.; He, L.; Pena, D. J.; Walton, I. D.; Cromer, R.; Keating, C. D.; Natan, M. J. *Science* **2001**, *294*, 137-141.

(3) Kovtyukhova, N. I.; Martin, B. R.; Mbindyo, J. K. N.; Mallouk, T. E.; Cabassi, M.; Mayer, T. S. *Mater. Sci. Eng., C* **2002**, *19*, 255–262.

(4) Woellenstein, J.; Plescher, G.; Kuehner, G.; Boettner, H.; Niemeyer, D.; Williams, D. E. *IEEE Sens. J.* **2002**, *2*, 403-408.

(5) Williams, D. E. *Sens. Actuators, B* **1999**, *57*, 1-16.

(6) Shimizu, Y.; Egashira, M. *MRS Builletin* **1999**, *24*, 18-24.

(7) Özgür, Ü.; Alivov, Y. I.; Liu, C.; Teke, A.; Reshchikov, M. A.; S. Doğan, V. A.; Cho, S. J.; Morko ç, H. *J. Appl. Phys.* **2005**, *98*, 041301-103.

(8) Goux, A.; Pauporté, T.; Chivot, J.; Lincot, D. *Electrochim. Acta* **2005**, *50*, 2239-2248.